Wiley
Geofluids
Volume 2026, Article ID 6180315, 22 pages
https://doi.org/10.1155/gfl/6180315

WILEY

*Research Article*

# Mineral Weathering Experiments for Terrestrial Planetary Analogs in a Continuous-Flow Reactor

**Jessica M. Weber**,[1] **Eduardo Martinez**,[1] **Rachel Y. Sheppard**,[2,3] **Laura E. Rodriguez**,[4] **Aaron Celestian**,[5] **Bronwyn L. Teece**,[1] **and Laura M. Barge**[1]

[1]*NASA Jet Propulsion Laboratory, California Institute of Technology, Pasadena, California, USA*
[2]*Planetary Science Institute, Tucson, Arizona, USA*
[3]*Institut d'Astrophysique Spatiale, CNRS, Université Paris-Saclay, Bures-sur-Yvette, France*
[4]*Lunar and Planetary Institute, Universities Space Research Association, Houston, Texas, USA*
[5]*Natural History Museum of Los Angeles, Los Angeles, California, USA*

Correspondence should be addressed to Jessica M. Weber; jessica.weber@jpl.nasa.gov

Received 10 July 2024; Revised 22 September 2025; Accepted 6 November 2025

Academic Editor: Pramita Mishra



Understanding the groundwater environments for ancient Mars and other terrestrial bodies is of great interest for evaluating their habitability. Here, we experimentally tested simulated aqueous alterations of two Mars simulants (variants of MGS-1) using a continuous-flow packed bed reactor, reacting with three ionic simulated groundwater analog solutions containing $MgSO_4$, $FeSO_4$, or LiCl to explore the impact of the aqueous alteration on the minerals. The minerals from these experiments were analyzed via Mars mission–relevant and field-relevant techniques (LIBS, Vis-NIR, and XRF). We demonstrated that the liquid collected from the column outflow and the solid samples were impacted by the alteration. With the MGS-1 standard, we found that sulfate mineral dissolution occurred in all tested experimental conditions; however, in cases with $FeSO_4$ and $MgSO_4$, dissolution of gypsum might have been disfavored. In addition, when the simulants were exposed to LiCl solution, Li was easily detectable by LIBS analysis of the residual mineral material. We then contextualize how these results could inform observations by ongoing Mars missions.

**Keywords:** aqueous alteration; flow; groundwater; laser-induced breakdown spectroscopy; lithium; weathering

## 1. Introduction

The aqueous environment and geofluids of ancient Mars are of great geochemical and astrobiological interest, with several ongoing landed missions oriented around constraining the geochemistry of the Martian surface and its ancient groundwaters. There is evidence across Mars for varied types of aqueous environments such as seas, oceans, deltas, valley networks, sapping channels, outflow events, and hydrothermal systems [1]. Each of these environments could introduce varied volumes of fluids over short to long periods, which could leave signals of varied strengths in the rock record [1]. In this paper, we focus on groundwater as all of the Martian rovers have observed evidence of former groundwater flow through subsurface rocks, including mineral dissolution, precipitation, and alteration [2–11]. There have been several studies into what alteration mineral assemblages might be present on Mars that could record evidence of water–rock reactions, such as Fe/Mg smectites, Al-bearing phyllosilicates, and chlorites (e.g., [12]). However, while the mineral assemblages in some systems have been identified, it is unclear what specific alteration products and groundwater composition would be produced from aqueous mineral weathering of whole-rock Mars simulant regolith from different brines. Better constraining these processes would increase our ability to contextualize mission data (from past missions, e.g., Spirit or Opportunity; ongoing missions, e.g., the Mars Curiosity Rover; or future missions, e.g., the Rosalind Franklin Rover) and determine how aqueous weathering products reflect the evolution of the Martian

landscape throughout its geologic history. Laboratory experiments simulating aqueous mineral interaction can allow us to predict what reactions took place in the early (~3–4 Ga), wet Martian surface/subsurface environments to explain the observed mineral assemblages. In particular, a crucial next step in improving our understanding of Martian geochemistry is constraining the mineral transformation pathways that likely occurred in groundwater episodes that may have had different chemistries through characterizing the resulting mineral precipitation/dissolution, which form secondary minerals. Subsurface environments exposed to groundwaters have been proposed as potential habitable regions due to protection from radiation/oxidation and availability of CHNOPS elements [12, 13]. Thus, identifying and characterizing past aqueous environments would be important for assessing past Martian habitability as well as the general understanding of geofluids. However, groundwater alteration in the Martian subsurface is difficult to directly observe with missions. Some observation methods include elemental abundance and mineralogy measurements through X-ray fluorescence (XRF) (PIXL on Perseverance and ChemMin on Curiosity), X-ray diffraction (XRD) (ChemMin), laser-induced breakdown spectroscopy (LIBS) (SuperCam on Perseverance or ChemCam on Curiosity), and infrared (IR) spectroscopy (SuperCam on Perseverance).

In this work, we conducted mineral alteration/weathering experiments to simulate water–rock interactions of Mars analog minerals with subsurface groundwater flows, using a type of continuous-flow reactor. Continuous-flow chemistry is a method where one or more reactants in aqueous solution are flowed through a tubing or pipe-based reactor, which may optionally contain solid reactive material in a porous packed bed. Continuous flow methods are commonly used in pharmaceutical chemistry to facilitate organic reactions [14, 15], and these methods are scalable and modular and have improved safety features compared to traditional batch chemistry. These systems have been utilized in industry to improve processes, especially as scalability allows for a wide range in volumes for these experimental setups. The time scales for these flow reactors can range from minutes to days, depending on the desired experiment. Another benefit of the continuous flow method is that the continuous-flow components are commercially available, making this technique cost-effective and adaptable in comparison to custom-built reactor systems.

A subset of continuous-flow chemistry—"flow-through" reactors, in which fluids flow through a solid (mineral) matrix—has been successfully utilized in the geosciences, including cases specifically relevant to Mars groundwater [16–20]. Previous work was primarily run at low pH and was often focused on clay materials. In addition, these experiments were commonly run on the time scale of hours to days and have been compared to related batch experiments (e.g., [20–22]). While these works have expanded the knowledge of potential groundwater systems on Mars, further mineral mixes and ionic solutions should be explored to have a full picture of the environment. Overall, the use of a contained laboratory system provides control of mineralogical composition and minimization of chemical and biological contamination. In addition, the use of modular parts allows for rapid setup, cleaning, and customization of experiments and ensures that the experimental setup can be readily replicated.

Flow reactors are inherently different than batch reactors since it is an open (vs. closed) system. The water interacting with the column generates some change in the matrix: Ions are dissolved and removed from one column and emplaced on another. The system will experience water flow, which would not occur in a batch reactor. The flow column in this work additionally provides an opportunity to examine heterogeneity (of approximately the top 8 cm of the column vs. the lower portion of the column; Figure 1) due to dissolution and redeposition of ions. This successive dissolution and precipitation at different places in a porous medium are aspects that can only be simulated in a flow experiment, not a batch experiment, where all solid material would be reacting with the fluid. In continuous-flow experiments, the bottom of the column has been more exposed to the water compared to the top, mirroring what we would expect with regolith exposed to ground waters compared to surface regolith. We hypothesize that the different simulants will exhibit different ion leaching behavior due to the different materials present and their solubility, as well as their particle size, and that the column will yield differences in composition along its length after flow reaction with fluid, as the bottom material will have more contact with the liquid.

In this study, we utilized continuous-flow methods for simulating low-temperature Martian geochemical conditions and demonstrate methodological value in examining Mars groundwater mineral weathering processes. We specifically investigate the interactions within a Martian-like groundwater system composed of a basaltic regolith and a flow through solution containing $Li^+$, $Na^+$, $Fe^{2+/3+}$, $Mg^{2+}$, $Cl^-$, and/or $SO_4^{-2}$. These groundwater system compositions are representative of conditions observed at terrestrial Mars analog sites. On Earth, ionic solutions interacting with basalt formations in volcanically active regions drive key physical and chemical processes that influence primary and secondary mineral formation. Weathering of basalt rocks leads to the release and mobilization of ionic species such as $Ca^{2+}$ and $Na^+$ and produces secondary phases including clay minerals, iron oxides/hydroxides, carbonates, and silica phases [23, 24]. In contrast, $Cl^-$ and $SO_4^{2-}$ are delivered via groundwater flow from surrounding environments, with $SO_4^{2-}$ capable of precipitating secondary sulfate minerals under acidic conditions with $H_2SO_4$ [25]. These processes are documented in basaltic systems such as the Columbia River Basalt Group (CRBG), Hawaii, and Iceland [23, 24, 26]. In Hawaii, basalt weathering leads to the release of $Li^+$ and the formation of clay minerals, where subsequent adsorption of $Li^+$ onto clay minerals occurs [26, 27]. Accordingly, this study considers a basalt–fluid environment to investigate the geochemical interactions that may have occurred on Mars and are observable in Mars analog settings.

We simulated various Mars groundwater compositions flowing through established Mars regolith simulants [28, 29]; analysis of the resulting altered minerals included mission-relevant techniques such as XRF, LIBS, XRD, and

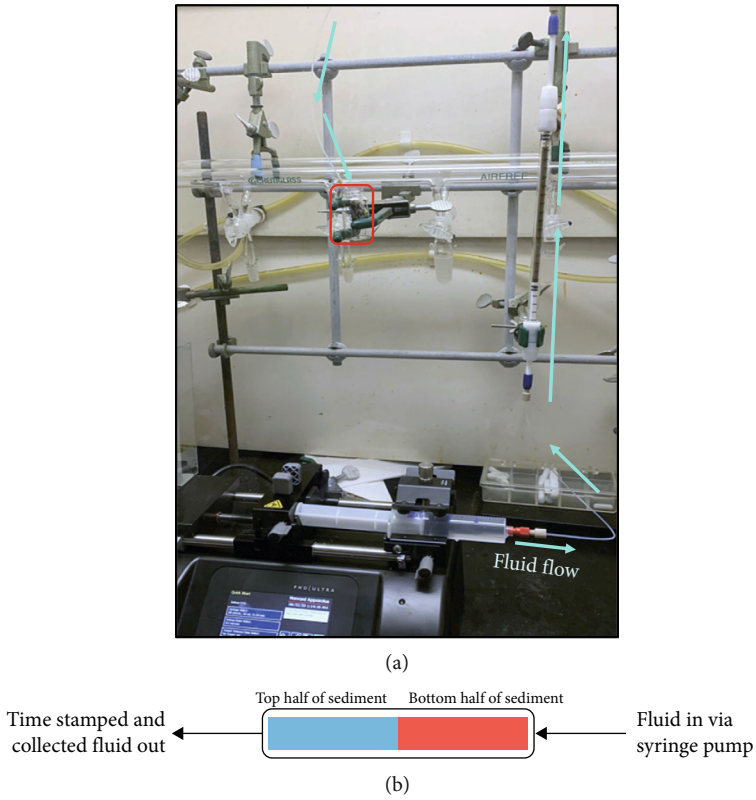


FIGURE 1: (a) Labeled photo/schematic of reactor setup with fluid flow direction indicated and the liquid sample collection indicated with a red box. (b) Description of the breakdown of the top and bottom of the packed bed. The top and bottom sections collected correspond to approximately the top and bottom 8 cm collected from the column.

visible-near infrared (Vis-NIR) reflectance spectroscopy. Our results demonstrate that groundwater flows can impact Martian sediments in a manner that is detectable using instrumentation that is presently in use on the Martian surface.

## 2. Methods

*2.1. Simulant Selection.* For our continuous-flow packed bed reactor, three commercially available Martian simulants were exposed to various ionic solutions to understand geochemical transformations and discern how aqueous weathering could impact the chemistry and composition of past groundwater systems. In these experiments, one of three Mars simulants was used to fill packed beds: (1) Exolith Lab's Mars Global Simulant (MGS)-1 [29], which was not altered in any way from the standard composition, hereafter referred to as MGS-1 standard; (2) a custom version of MGS-1 prepared by Exolith Lab with only the coarser grain size components (see Supporting Information for more information), hereafter referred to as MGS-1 coarse; and (3) Mojave Mars Simulant (MMS) [30] (see Figure S5 for chemistry, mineralogy, and particle distribution curves for on these three simulants). MMS was designed as a primarily geophysical simulant with crystalline phases including feldspar, olivine, pyroxene, anhydrite, ferrihydrite, goethite, quartz, and magnesite [30]. The MGS-1 mixtures are mineral simulants that are designed to replicate the global Martian basaltic regolith, with a focus on the Rocknest deposits on Gale Crater [29], although remote and in situ data indicate a relatively homogenous chemical composition of the global regolith [28]. While the MGS-1 coarse and the MGS-1 standard are similar, they do not have identical compositions; the MGS-1 coarse lacks the smaller materials in the MGS-1 standard. MGS-1 coarse was chosen out of concern to not clog the column apparatus and to explore the impacts of the finer grained, amorphous material.

The three regolith simulants used in these experiments exhibit distinct particle size distributions that affect fluid flow and reactive surface area differently.

MMS has a bimodal particle size distribution, spanning 1.5–1500 $\mu$m, with a small peak at 10 $\mu$m ($q \approx 1.5\%$) and a larger peak at 400 $\mu$m ($q \approx 7\%$) (Figure S5a). The presence of fine-grained material, including clay-sized particles, increases reactive surface area but also enhances the potential for pore clogging, which can limit fluid transport and alter reaction kinetics.

MGS-1 spans a similar particle size range (1.5–1500 $\mu$m) but exhibits a trimodal distribution, with peaks at 15 $\mu$m ($q \approx 3.5\%$), 80 $\mu$m ($q \approx 2.8\%$), and 700 $\mu$m ($q \approx 3.4\%$) (Figure S5b). The greater proportion of fine particles compared to MMS suggests an increased reactive surface area but also an elevated risk of permeability reduction due to particle mobilization and deposition within pore spaces.

MGS-1 coarse, a modified version of MGS-1 designed to reduce clogging, has a unimodal particle size distribution

spanning 400–4500 $\mu$m, with a peak centered at 1200 $\mu$m ($q \approx 17\%$) (Figure S5c). The absence of finer particles significantly reduces available surface area for reactions but improves permeability and prevents reactor clogging, ensuring more consistent flow-through conditions.

These variations in particle size distribution directly influence reaction rates, as finer grained materials provide greater reactive surface area but also increase the likelihood of flow restriction due to particle settling and pore clogging. In contrast, coarser grained materials, while facilitating fluid flow, limit the total surface area available for reactions, potentially slowing overall reaction kinetics. MGS-1 coarse was chosen out of concern to not clog the column apparatus. As MGS-1 is a modified version of the Rocknest-based MGS-1 simulant, it may be more relevant to coarser grained sedimentary deposits associated with fluvial or deltaic deposits that experienced less chemical weathering, but we propose that it is still appropriate to explore Noachian-to-Hesperian Martian conditions, as coarse-grained size (1 mm particles) has been observed in areas within Gale Crater [31].

*2.2. Geologic Setting.* We explored groundwater analog solutions containing dissolved $MgSO_4$, $FeSO_4$, or LiCl. These salts were chosen since their anions and cations are relevant to estimates of Noachian–Hesperian Mars groundwater conditions, which are expected to have been richest in $Fe^{2+/3+}$, $Mg^{2+}$, $Ca^{2+}$, $Al^{3+}$, $Na^{+}$, $K^{+}$, $Cl^{-}$, $HCO_3^{-}$, and $SO_4^{2-}$ [32, 33]. We also included Li because Li appears elevated in clay-rich terrains in Gale Crater, and concentration has been proposed as a proxy for clay mineral content [34, 35]. Although Gale Crater contains diagenetically altered sediments, the precise water chemistry and source are still unclear [36], with investigations ranging from a surficial ice source [37], deep upwelling groundwater [38], or impact-induced hydrothermal systems [39]. The Curiosity rover is currently exploring sulfate-rich strata in Mt. Sharp, so sulfate solubility, transportability, and chemistry postreprecipitation are all of great interest to interpret data from the mission [40–42], especially as the connection between sulfates and organic preservation on Mars is a guiding beacon for habitability [43–45]. $SiO_2$ is also expected to be a primary component of early Martian groundwater [32, 33] but was omitted from our groundwater simulant out of concern for precipitation and clogging the apparatus. We focused on the impacts of individual ionic materials on the Martian analogs and did not explore a mixed groundwater solution, as we were interested in exploring the impact of the specific reagents. pH of the initial solutions was measured in duplicate with pH strips.

### 2.3. Experimental Protocol

*2.3.1. Reactor Setup.* Weighed simulant was placed into a Diba Omnifit EZ Chromatography Column (with one fixed and one adjustable end piece) to create a packed bed, which was secured vertically with clamps inside a fume hood. This packed bed column was connected with a 0.03-in. id tubing on the lower end to a Harvard syringe pump and on the upper end to a liquid collection vessel (either a 20-mL glass vial or 15-mL Falcon tube) (Figure 1). A plastic 30-mL syringe was used to inject the desired analog groundwater solution into the bottom of the packed bed. In initial experiments, only pure Milli-Q water was injected as a control, and then, in later tests, one of three different ionic solutions was injected (50 mM $MgSO_4$, 50 mM $FeSO_4$, or 50 mM LiCl) into a packed bed of MGS-1 standard or MGS-1 coarse (Table 1). (MMS clogged the column during the water control run and so could not be used further in this study.) For all solutions, pH was measured but not adjusted or buffered, as we were exploring specific ion impact on the mineral species. In addition, these solutions were made open to the air, and no attempt to replicate a Mars atmosphere was made. Therefore, the solutions were exposed to oxygen. As a note, this would cause oxidation of the Fe material over the course of time. This would impact the iron mobility and redox-sensitive elements present within the experimental setup. All experiments were run at room temperature.

The flow/injection rate was set to 0.2 mL/min for the experiment (unless otherwise noted), and the packed beds were never allowed to run dry; for consistency and to avoid any flushing of materials out of the column at the end of the experiment, every experiment was stopped with fluid still in the syringe. A 0.2 mL/min was chosen in order to collect sufficient material at 15-min time points for liquid analysis. The experiments were run over the course of 1.5–3 h, which is on a relatively short time scale but is comparable to time points taken during some batch experiments. This flow rate allowed for sampling substantial fluid for analysis on the minute time scale while also allowing for a full syringe to be used in one setting on the hour time scale. This flow rate also did not clog the MGS-1 analogs. In addition, three other flow rates (0.5, 1.0, and 2.0 mL/min) were explored with 50 mM LiCl to determine if flow rate had an impact on alteration. Additional information about all experimental runs is included in the Supporting Information (Table S1). The experiments were run for 2–3 h with at least four time points collected to determine how quickly alteration would be observed in these systems. For these experiments, we were focused on short-term alterations (e.g., on the scale of minutes to hours), and this is in line with previous batch experiments, including Elwood Madden [21]. This flow rate allowed for the collection of enough liquid sample at multiple 15–30-min time points (e.g., sampling at 15 and 30 min and 1 h). Increasing the flow rate would alter the time points taken and the amount of liquid that could be collected.

The packed bed was fully injected with liquid prior to beginning the experiment. The run timer was started once the reactor was fully filled to avoid delays in collecting liquid samples. The reactions were run for 1–3 h at ambient temperature and pressure, and time-stamped liquid samples were collected at different intervals throughout the experiment. A $t = 0$ time point, a sample of the original liquid used in the experiments, was taken. These liquid samples were frozen in a −20°C freezer for anion ion chromatography (IC) analysis. The solutions were frozen within approximately 10 min after the time point was collected. No filtration was performed to process these samples prior to freezing or preparing for IC analysis.

**TABLE 1**: Table of experiments that were conducted with different simulants and salt solutions. X indicates that experiments were performed under these conditions. All reactions were run in duplicate. We also describe codes for our experiments. Keys: C = MGS-1 coarse; S = MGS-1 standard; W = Milli-Q water; M = $MgSO_4$; F = Fe(II)$SO_4$; L = LiCl; T = top; B = bottom. All experiments were run in at least duplicate. Further information about the experimental list can be seen in Table S1 in the Supporting Information.

| Ionic solution (abbreviation) | Average pH of the solution | MMS | MGS-1 standard | MGS-1 coarse |
|---|---|---|---|---|
| Milli-Q water (W) | 6.5 | X (clogged) | X (W-S-T/B) | X(W-C-T/B) |
| 50 mM $MgSO_4$ (M) | 7.0 | N/A | X (M-S-T/B) | X (M-C-T/B) |
| 50 mM $FeSO_4$ (F) | 5.0 | N/A | X (F-S-T/B) | X (F-C-T/B) |
| 50 mM LiCl (L) | 7.25 | N/A | X (L-S-T/B) | X (L-C-T/B) |

Upon completion of the reaction, an ambient air-filled syringe was injected to expel fluid and dry the packed bed as much as possible. Altered simulants were removed from the 8 cm top and bottom components of the packed bed (and the sediments were kept separated) (Figure 1).

These simulants were stored in 15-mL Falcon tubes inside an oxygen-free Coy glovebox to air dry for XRF, XRD, LIBS, and IR analyses to prevent any oxidation change during their drying and storage. Postexperimental analyses were conducted on the solid phases and the liquid outflow samples. All mineral samples were analyzed via VNIR and LIBS. All liquid samples were analyzed via anion chromatography. The only time select samples were used were for XRF and XRD.

### 2.4. Liquid Analysis

*2.4.1. IC.* The time-stamped liquid samples were analyzed via anion IC. With the current setup of this system, only anionic materials can be measured. IC data were obtained with a Thermo Scientific Dionex Integrion HPIC equipped with a Dionex IonPac AG11-HC-4 $\mu$m column (4 × 250 mm). All 15- or 30-minute time-stamped collection vials were sampled and treated in four steps. First, 0.1 mL was sampled and diluted with 0.4 mL of deionized Milli-Q water (5× dilution) in Eppendorf tubes and centrifuged for 2 min. Then, 0.4 mL of the supernatant was sampled and mixed with 0.1 mL of 1 M NaOH (to precipitate any dissolved metals from solution, 0.25× dilution), vortexed, and centrifuged again. Next, 0.4 mL of the resulting supernatant was injected through a 0.2 $\mu$m filter (Avantor) into new Eppendorf tubes. Lastly, 0.25 mL of the filtered supernatant was diluted with 4.75 mL of deionized Milli-Q $H_2O$ (20× dilution, 5 mL total volume injection into IC) in PolyVials.

After this last step, each new sample was loaded into an AS-DV autosampler and injected individually for a total of 15 min. Standards of the solutions (i.e., samples of the ionic solutions not run through the column) were also taken and treated in the same manner. The samples were injected into the IC using an isocratic flow rate of 1.25 mL/min using an EGC 500 KOH eluent set to 30 mM. The data of the anion chromatograms were exported into Excel, and the conductivity ($\mu$S) was multiplied by the dilution factor (e.g., 5 × 0.25 × 20) of the sample treatment. The final conductivity ($\mu$S) versus time (min) was plotted using Veusz (Figures S6–S23).

### 2.5. Solid Analysis

*2.5.1. LIBS.* Dried samples of the Mars simulants from the packed bed postexperiment were further powdered using a mortar and pestle, placed in a die, and made into 13-mm-diameter pellets by applying 8 t of force for 10 min using a manually operated benchtop 12-t SpectroPress (4312, Chemplex Industries, Inc.). Pellets were analyzed using a custom lab-grade LIBS chemical imaging system built by Impossible Sensing (1060 nm Red Energy Fiber laser, 20 W at 33 kHz). Settings were optimized for the analysis of these particular samples (250 shots, pulse repetition frequency: 20,000 Hz). Each sample was analyzed at 10–20 different locations to minimize variation due to the analysis.

*2.5.2. LIBS Processing.* The spectrometer used to collect LIBS spectra is composed of three spectrometers that collect from the near-UV, visible, and near-IR regions. All data were processed using the R software. As each region has a different signal-to-noise ratio and background, each of the three regions was preprocessed separately before being combined to generate a single spectrum. Preprocessing involved trimming the overlapping ends of each spectrum, denoising using the *wavshrink* function in the *wtmsa* package [46, 47], and correcting for the Bremsstrahlung effect on the baseline using the rollingBall method in the *baseline* package [48]. The rollingBall method is conceptually similar to a sphere that moves along the base of the peaks to establish their height relative to the baseline and is used in LIBS studies due to the nonlinear peak base heights relative to baseline (e.g., [49]). The three regions were then combined to form a single spectrum. To correct for intensity changes due to inherent shot-to-shot variations and matrix effects, each spectrum was normalized to the sum intensity over the entire spectrum.

*2.5.3. Calculating Peak Areas.* Peaks were deconvoluted using the Levenberg–Marquardt optimizer (*nlsLM* function in the *minpack.lm* package; [50]) to fit a pseudo-Voigt function to a narrow (~2–6 nm) spectral window centered at a preselected peak of interest [51]. This process searches for fits to several parameters in the pseudo-Voigt equation that optimizes the fit with the raw data. The parameters describe each peak and include the peak center (nm), intensity, full-width half max, and the proportion of Gaussian to Lorentzian. The number of peaks, as well as a starting guess and constraints for each parameter, was derived for each spectral

window using a homemade R script that leverages first and second derivatives of the narrow spectrum of interest. Fits that had a root mean square error > 0.1 were considered a poor fit and not used in subsequent analyses. The deconvolved peaks were integrated to calculate the area.

*2.5.4. Statistical Analyses.* For each sample, areas that fell outside 1.5× the inner quartile range were considered outliers and removed. Analysis of variance (ANOVA) was performed on the means of experimental replicates to determine if there were significant differences in the areas for elements of interest due to the solution passed through the column (none, water, 50 mM $MgSO_4$, 50 mM $FeSO_4$, and 50 mM LiCl), the location of the sample (being at the bottom vs. the top of the column), or the simulant used (MGS-1 coarse vs. MGS-1 standard). For factors (i.e., solution, sample location, and simulant) showing a significant effect in ANOVA, we conducted Tukey-adjusted post hoc pairwise comparisons of estimated marginal means to identify specific group differences (e.g., MGS-1 exposed to water vs. MGS-1 exposed to $FeSO_4$) [52].

*2.5.5. Peak Deconvolution.* The 13 elements of interest for LIBS analysis were selected based on their abundance in the MGS-1 simulants (Figures S33–S37) and ionic solutions used in this study. Of the 13 elements, 11 had emission lines suitable for further analysis (see Table S2 for details). Suitability criteria for further processing included the following: (i) The emission line matched a known and relatively strong emission line from the NIST database, (ii) the emission line was in a region with minimal interferants (i.e., only the element of interest produced a good signal at the isolated emission line) from other elements present in the MGS-1 simulants, and (iii) changes in mean intensity of the emission line per experiment were consistent with elemental changes based on XRF analysis of the same sample experiment (Runs 2—MGS-1 coarse + water; 3—MGS-1 coarse + $MgSO_4$; 5—MGS-1 standard + water; 7—MGS-1 standard + $MgSO_4$; and 8—MGS-1 coarse + LiCl). For peak deconvolution, there was an additional requirement that the peak did not experience significant peak broadening between samples (as this hindered deconvolution efforts). Visual inspection of a subset of selected spectra from each experiment for each element that was deconvolved revealed that the algorithm was able to optimize a pseudo-Voigt function to the peaks with sufficient accuracy (mean RMSE for all elements = 0.03); the mean RMSE corresponding to each peak is shown in Table S2.

*2.5.6. Vis-NIR Reflectance Spectroscopy.* Vis-NIR reflectance spectra were collected using an Analytical Spectral Devices (ASD) FieldSpec spectroradiometer spanning 0.35–2.5 $\mu$m on both the reacted powders and control samples of the original minerals. Vis-NIR reflectance spectra of the samples were collected prior to grinding and pelleting for LIBS. Spectra were acquired using a fiber optic cable situated in a contact probe grip and relative to a Spectralon white reference. Solid samples were dried but not powdered and placed on Cinefoil matte black sample paper for data collection.

Relevant Vis-NIR band depth parameters were calculated using the methods of Clark and Roush [53], where a piecewise linear fit was used to define the spectral continuum. Band depth measurements can provide a comparative measure of absorption strength between samples, where a band depth of 0 signifies a characteristic absorption is absent and a band depth of 1 signifies an absorption is saturated. Several features, including particle size and mineral opacity, can influence band depth. Because the particle size distribution and mineralogy before the experiments were standardized (i.e., all MGS-1 standard experiments had the same starting characteristics), comparing band depth among samples run on the same simulant is a useful way to compare mineral changes induced by the run. The SINDEX spectral parameter [54] was also calculated for each sample (Figures S25 and S29). SINDEX is a measure of spectral characteristics consistent with sulfate abundance, specifically a spectral convexity > ~ 2.2 $\mu$m related to a drop in reflectance due to the strength of a broad absorption of ~2.4 $\mu$m [54–56].

*2.5.7. XRD.* Dried and powdered samples were processed by XRD, and their patterns were collected using a Proto AXRD with Cu radiation and equipped with a 128-channel Dectris linear detector. Data were collected using step scans of 0.02° and 2-s dwell per step. XRD patterns were collected for sediment from a subset of runs. All sediment examined using XRD was from the top position in the packed bed, and the sediment was dried and powdered using a mortar and pestle to a consistency of flour. Samples were then adhered to a glass plate (smear mount) with EtOH. Mineral phases were identified using the JADE software package with whole pattern fitting. JADE (developed by Materials Data, Inc.) is a specialized XRD analysis software that integrates database searching, peak fitting, and Rietveld refinement capabilities. The software employs a comprehensive pattern-matching algorithm that compares experimental diffraction patterns against reference databases such as the ICDD PDF-4+ or AMCSD (American Mineralogist Crystal Structure Database).

For quantitative mineral abundance analysis, JADE implements the Rietveld refinement method by constructing a theoretical diffraction pattern from crystallographic information files (CIFs) of identified phases. The software iteratively refines structural parameters (unit cell dimensions, atomic positions, and thermal factors) and profile parameters (peak shape functions, background, and preferred orientation) to minimize the difference between calculated and observed patterns. JADE's implementation uses a damped least-squares algorithm that optimizes the scale factors for each phase, which are directly proportional to the weight fractions of the constituent minerals in the sample. The refinement quality is assessed through statistical indicators, including the weighted profile *R*-factor (Rwp) and goodness-of-fit ($\chi^2$), with values below 10% for Rwp typically indicating acceptable fits. Phase quantification accuracy is further enhanced by JADE's ability to model microstructural effects such as crystallite size and strain broadening

using the fundamental parameter approach, which considers instrumental broadening contributions separately from sample-related effects.

*2.5.8. XRF.* Three XRF spectra were collected for select post-run, dried samples. A small amount of each sample was placed inside a capillary tube, and spectra were collected using a Horiba XGT-7200 micro-XRF with a 1.2 mm beam size. A total of three spectra were obtained per sample, and all the spectrum results were averaged to provide the final abundance measurement. Qualitative elemental abundances were determined using a fundamental parameters peak-fitting model for all spectra as implemented in the XGT-7200 software.

## 3. Results

*3.1. Fluid Analysis.* Milli-Q water was first employed as a control to determine the feasibility of flow through experiments with these simulants, as well as to get a baseline for any mineralogical changes. We found that the water flow rate was significantly slowed in packed beds filled with MMS, including repeats, such that the experiments were clogged and ended in under 1 min. Mineral samples and water from the packed bed were collected for these runs. Packed beds filled with MGS-1 standard (W-S) and MGS-1 coarse (W-C) were able to sustain flowing water for the duration of the entire experiment. Based on these results, we did not conduct further flow experiments with MMS.

The IC results from experiments performed with MGS-1 coarse and DI $H_2O$ (W-C) reveal minor peaks associated with our DI $H_2O$ and MGS-1 coarse regolith (all IC results shown in Figures S6–S23). While the Milli-Q water is ultrapure, the IC is sensitive enough to detect trace ions in the water, so this is not unexpected. The results of Run 2 and Run 10 show that the conductivity of the analytes is < 200 $\mu$S where the peaks belong to organic acids from 2.20 to 2.80 min, $F^-$ from 3.55 to 3.75 min, $Cl^-$ from 3.95 to 4.70 min, $SO_4^{2-}$ from 4.85 to 5.20 min, and $NO_3^-$ from 6.85 to 7.20 min (Figure 2a,b). In Run 10, a broadened peak of $Cl^-$ is observed from approximately 3.75 to 4.60 min. In experiments containing $MgSO_4$ and $FeSO_4$, the major anion peaks from our groundwater flow solutions (e.g., $SO_4^{2-}$ and $Cl^-$) and minor peaks from our DI $H_2O$ and MGS-1 coarse are observed. The experiments containing either $MgSO_4$ (M-C) or $FeSO_4$ (F-C) show a $SO_4^{2-}$ peak at 4.70 min (Figures 2c, 2d, 2e, and 2f). In experiments with $MgSO_4$ and MGS-1 coarse (M-C), the conductivity of the $SO_4^{2-}$ reached 7270.87and 4413.34 $\mu$S for Run 3 and Run 17, respectively (Figure 2c,d). In Run 17, minor peaks of $F^-$ and $Cl^-$ are evident and are similar to our DI $H_2O$ and MGS-1 coarse experiments (Figure 2d). In Run 4 and Run 22 with $FeSO_4$ and MGS-1 coarse (F-C), a spike in $SO_4^{2-}$ reached a conductivity measurement of 8429.26 $\mu$S in Run 4 and 4681.16 $\mu$S in Run 22 (Figure 2e,f). In Run 22, a minor $Cl^-$ peak is shown, similar to our DI $H_2O$ and MGS-1 coarse experiments (W-C). The anion from LiCl and MGS-1 coarse experiments was $Cl^-$ at ~3.46 min, a slight shift from our other runs, where the conductivity of the peak was 3732.98 $\mu$S in Run 8 and 3085.65 $\mu$S in Run 20. In the LiCl and MGS-1 coarse experiments, we observed a minor peak with a conductivity of ~25–500 $\mu$S of $SO_4^{2-}$ peak in Run 8 and Run 20, which is larger than the potential $SO_4^{2-}$ background peak observed in the DI $H_2O$ experiments (~0–60 $\mu$S after subtracting the baseline; Figure 2g,h).

Experiments performed with MGS-1 standard and DI $H_2O$, $MgSO_4$, $FeSO_4$, and LiCl show an $SO_4$ peak (appearing at 4.45 min) in every sample, regardless of the composition of the fluid (i.e., even when the simulant was exposed to Milli-Q water alone) (Figure 3). This is consistent with the composition of the MGS-1 standard simulant. In all experiments, the "flush" occurs between 0 and 15 min of the experiment, after the $SO_4^{2-}$ decreases drastically in magnitude for the rest of the experiment. In our Milli-Q $H_2O$ and MGS-1 standard simulant, the conductivity decreased from 21,862.28 $\mu$S at 15 min to 5686.09 $\mu$S in 30 min in Run 5 and from 31,620.72 $\mu$S in 15 min to 6655.55 $\mu$S in 30 min for Run 13, and the conductivity further decreased over time (Figure 3a,b). In experiments with $MgSO_4$ and $FeSO_4$, the $SO_4$ peak increased, given the composition of our solution. In experiments with $MgSO_4$, the $SO_4$ peak reached 49,135.62 $\mu$S at 15 min and decreased at 30 min to 8136.53 $\mu$S in Run 7. Similarly, in Run 21, the $SO_4$ peak reached a conductivity of 30,173.08 $\mu$S at 15 min to 5364.45 $\mu$S at 30 min (Figure 3c,d). In $FeSO_4$ and MGS-1 standard simulant, Run 18, the $SO_4$ conductivity reached 32,446.36 $\mu$S at the beginning of the experiment (0 min) and decreased to 8560.92 $\mu$S at 15 min, while Run 23 peaked at 31,563.19 $\mu$S and Run 24 peaked at 22,744.37 $\mu$S, and both decreased to 9428.07 and 10,258.73 $\mu$S at 15 min, respectively. Lastly, in the experiments with LiCl and MGS-1 standard (L-S), the $SO_4$ peak also appeared at magnitudes greater than the expected Cl peak. In Run 9, the $SO_4$ peak reached a maximum of 24,373.23 $\mu$S at 15 min and decreased to 5227.47 $\mu$S at 30 min. In Run 19, the $SO_4$ peak reached 24,947.67 $\mu$S and decreased to 3891.66 $\mu$S at 90 min (Figure 3i).

### 3.2. Solid Analysis

*3.2.1. Vis-NIR Reflectance Spectra.* The final Vis-NIR reflectance spectra of dried simulant were strongly affected by the type of simulant, the fluid composition, and the position within the packed bed (Figure 4). The MGS-1 coarse simulant spectra are dominated by a broad 1 $\mu$m feature associated with pyroxene, 1.4 and 1.9 $\mu$m vibrational features associated with structural water (likely in clay, sulfate, and X-ray amorphous phases), and a sharp absorption ~2.3 $\mu$m that is a metal–OH absorption consistent with clay minerals. This metal–OH absorption moves wavelength position depending on the cation, which can be seen most clearly in the continuum-removed spectra (Figure S24). The bottom of the packed bed has a stronger 2.3 $\mu$m absorption in all experiments except in the case of MGS-1 coarse + $MgSO_4$ (M-C; Run 3) and MGS-1 coarse + $FeSO_4$ (F-C, Run 4) (Figures S27b, S27c, and S27l). Spectral features associated with sulfate were also affected by the continuous-flow experiments (Figure S25). SINDEX values indicative of the presence of sulfates were

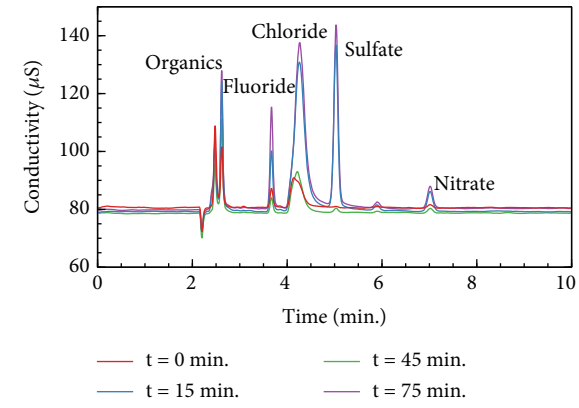


(a) Run 2: W-C

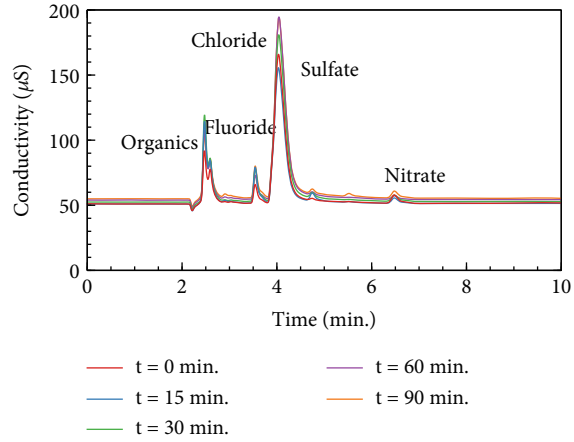


(b) Run 10: W-C

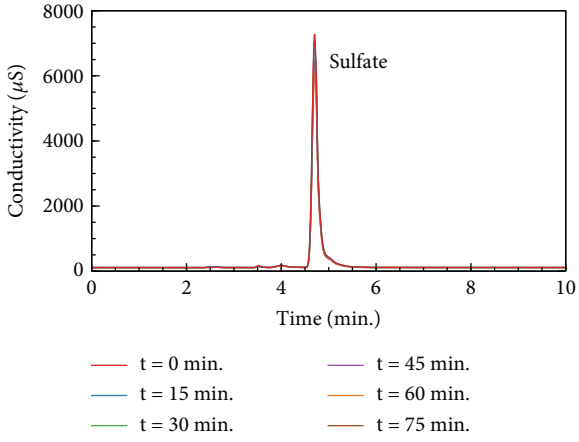


(c) Run 3: M-C

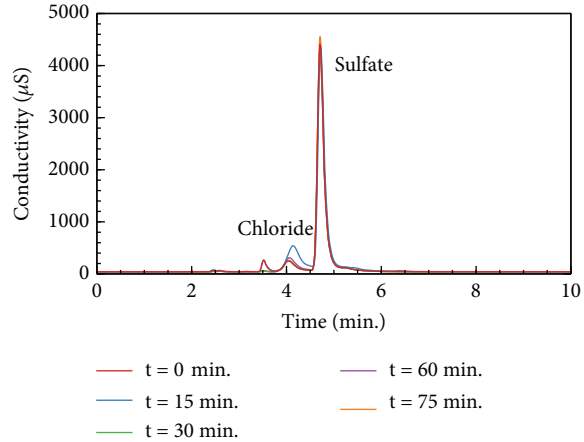


(d) Run 17: M-C

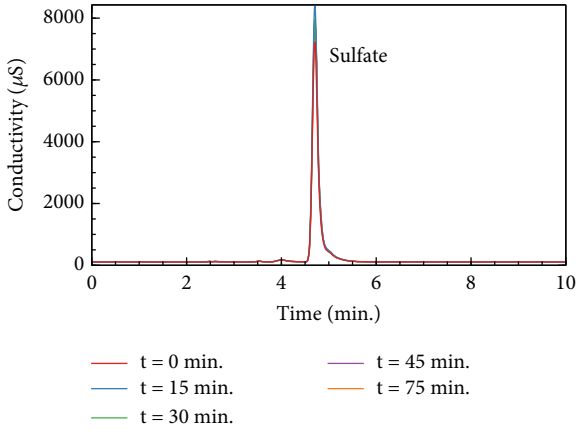


(e) Run 4: F-C

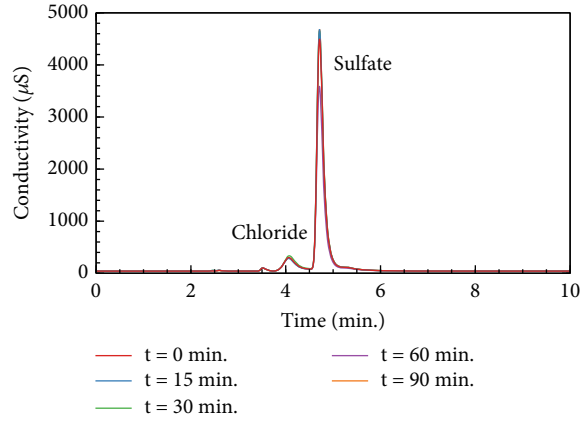


(f) Run 22: F-C

Figure 2: Continued.

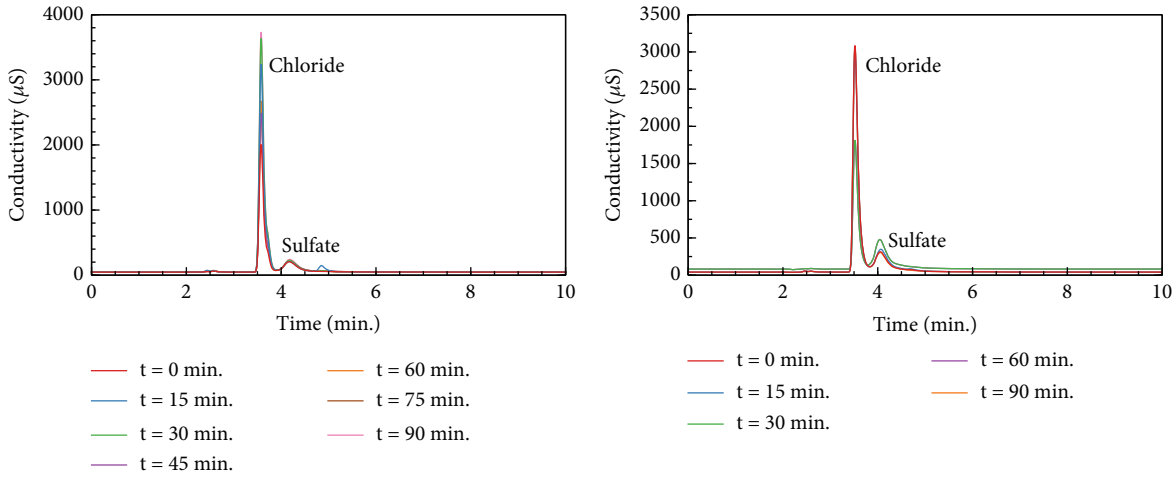


(g) Run 8: L-C (h) Run 20: L-C

FIGURE 2: Comparison of the ion chromatographs for the MGS-1 coarse experiments. All key peaks correspond to the anions added into the solution. Each row compares the spectra from a replicate experiment. Subtitle legend: C = coarse simulant exposed to solutions of W = water (no added salts), M = $MgSO_4$ solution, F = Fe(II)$SO_4$ solution, or L = LiCl solution. Note t0 is the solution control before exposure to the mineral simulant.

higher in the bottom of the packed bed in all experiments except MGS-1 coarse + $MgSO_4$ (Run 3) and MGS-1 coarse + $FeSO_4$ (Run 4) (Figures S26b, S26c, and S26l).

In experiments using MGS-1 standard simulant, the spectra were dominated by electronic absorptions associated with Fe (~0.4 and 0.9 $\mu$m), weak 1.4 and 1.9 $\mu$m vibrations associated with structural water, and a sharp absorption at ~2.3 $\mu$m that is a metal–OH absorption consistent with clay minerals (Figure S24). The continuum-removed metal–OH absorption was affected by some experiments but not others: The 2.3 $\mu$m band depth was largely unchanged in the pure water experiments (Runs 5 and 13) and significantly higher in the bottom of the packed bed in MGS-1 standard + $MgSO_4$ (M-S-T/B; Runs 7 and 21), MGS-1 standard + LiCl (L-S-T/B; Run 19), and MGS-1 standard + $FeSO_4$ (F-S-T/B; Runs 23 and 24) (Figure S24b,d). There were variations across the experiment, which were exceptions to the features noted above, as observed in the experiments with L-S-T/B runs: Run 9 is a duplicate of Run 19, and the 2.3 $\mu$m band was close to identical in both top and bottom. This variation was also seen in MGS-1 standard + $FeSO_4$ (F-S-T/B) Run 18, which is a duplicate of Runs 23 and 24, and the 2.3 is very shallow. This feature could be reflective of variability within the heterogenous mix of the sediment. SINDEX values were higher at the top of the packed bed in MGS-1 coarse + water (W-C-T/B; Run 5) and MGS-1 standard + $FeSO_4$ (F-S-T/B; Run 18) and were higher in the bottom of the packed bed in the rest of the experiments (Figure S25).

### 3.2.2. LIBS Elemental Analysis

*3.2.2.1. Statistical Analysis of LIBS Elements.* Upon exposure to water, the MGS-1 standard lost less K from the top of the column compared to the bottom; for MGS-1 coarse, the difference in loss between the two halves was negligible (Figure 5). For coarse MGS-1, only Fe was removed with the passing water in both the top and bottom columns relative to the dry control ($p < 0.05$). Water had the reverse effect on the Na, Al, and Ca content, increasing their intensity, with more in the top half compared to the bottom half of the column with MGS-1 standard simulant (Na: $p = 0.02$; Al: $p = 0.04$; and Ca: $p < 0.001$). In the bottom of the packed bed, Ca levels of the water-exposed MGS-1 standard had decreased relative to the starting amount; however, this change is not statistically significant. For the water-exposed MGS-1 coarse simulant, Al also increased in the top half of the packed bed ($p = 0.05$); differences in the Na and Ca content exposed to water compared to the unaltered MGS-1 coarse simulant were not found to be statistically significant. The effect on Li appears to be reversed between the simulants, with an increase in Li in the MGS-1 standard simulant ($p = 0.07$) and a decrease in Li in the MGS-1 coarse ($p = 0.01$ ) when exposed to water. Finally, the Mn content at both the top and bottom of the packed bed increased for the MGS-1 coarse but not the MGS-1 standard simulants; however, this change was not statistically significant ($p = 0.12$).

After considering the variability in the data, there appeared to be no significant changes in the elemental abundances for the MGS-1 standard simulant exposed to $FeSO_4$-containing waters. However, for the MGS-1 coarse simulant, exposure to $FeSO_4$ led to an increase in Al and Mn at both the bottom and top positions (Al: $p < 0.01$ and Mn: $p < 0.001$). Mg and Fe also decreased significantly in samples exposed to $FeSO_4$ waters (Mg: $p < 0.001$ and Fe: $p < 0.001$). Exposure to $MgSO_4$ solution led to an increase in the Al signal for both the MGS-1 coarse ($p = 0.04$) and standard simulants ($p = 0.1$), although the difference was only statistically significant for MGS-1 coarse sediments. Additionally, K, Fe, and Mg intensities decreased, while the Mn peak increased in the MGS-1 coarse sediments (K: $p = 0.07$; Fe: $p < 0.001$; Mg: $p = 0.03$; and Mn: $p < 0.01$); for the MGS-1 standard simulants,

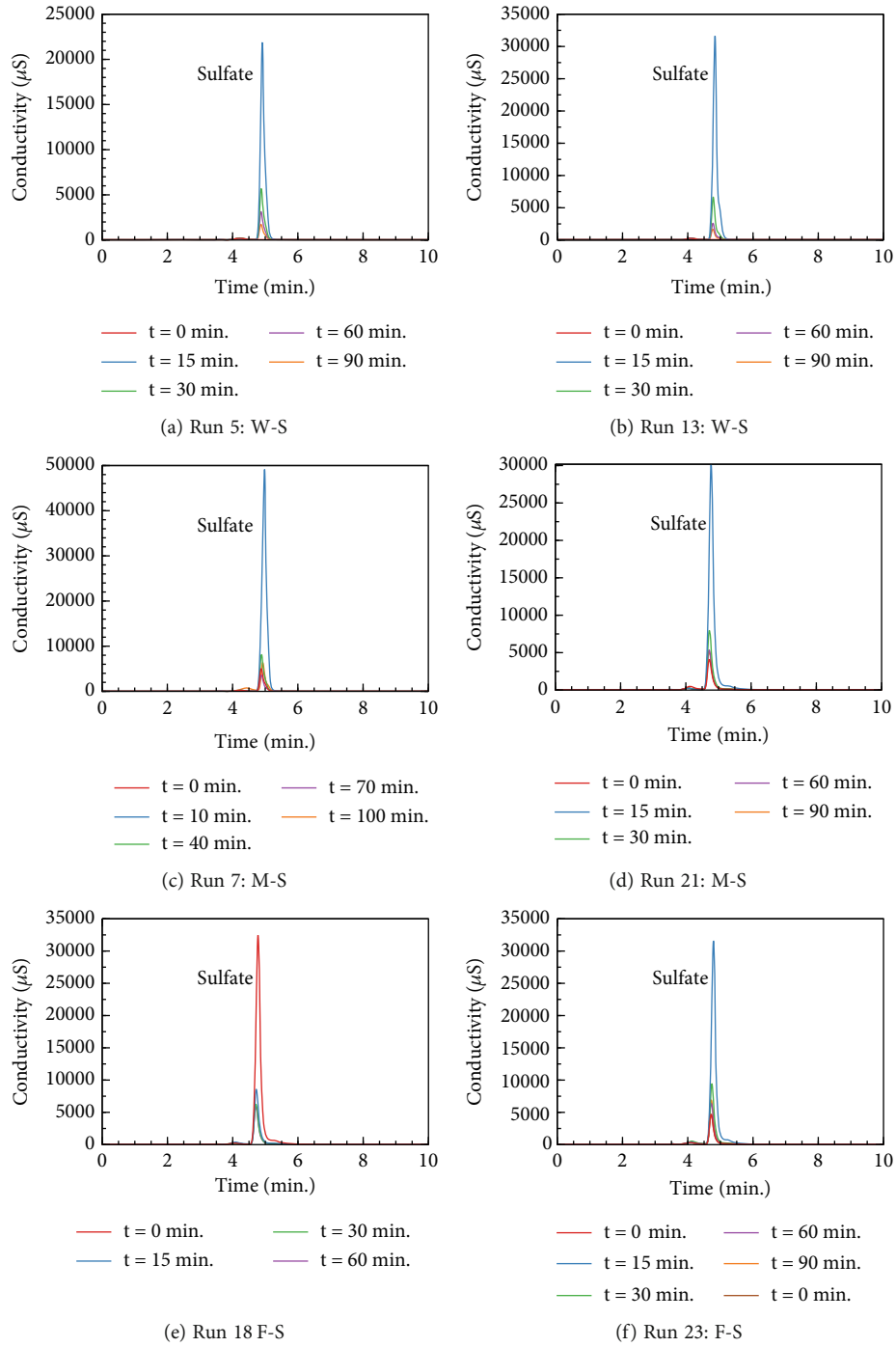


(a) Run 5: W-S

(b) Run 13: W-S

(c) Run 7: M-S

(d) Run 21: M-S

(e) Run 18 F-S

(f) Run 23: F-S

Figure 3: Continued.

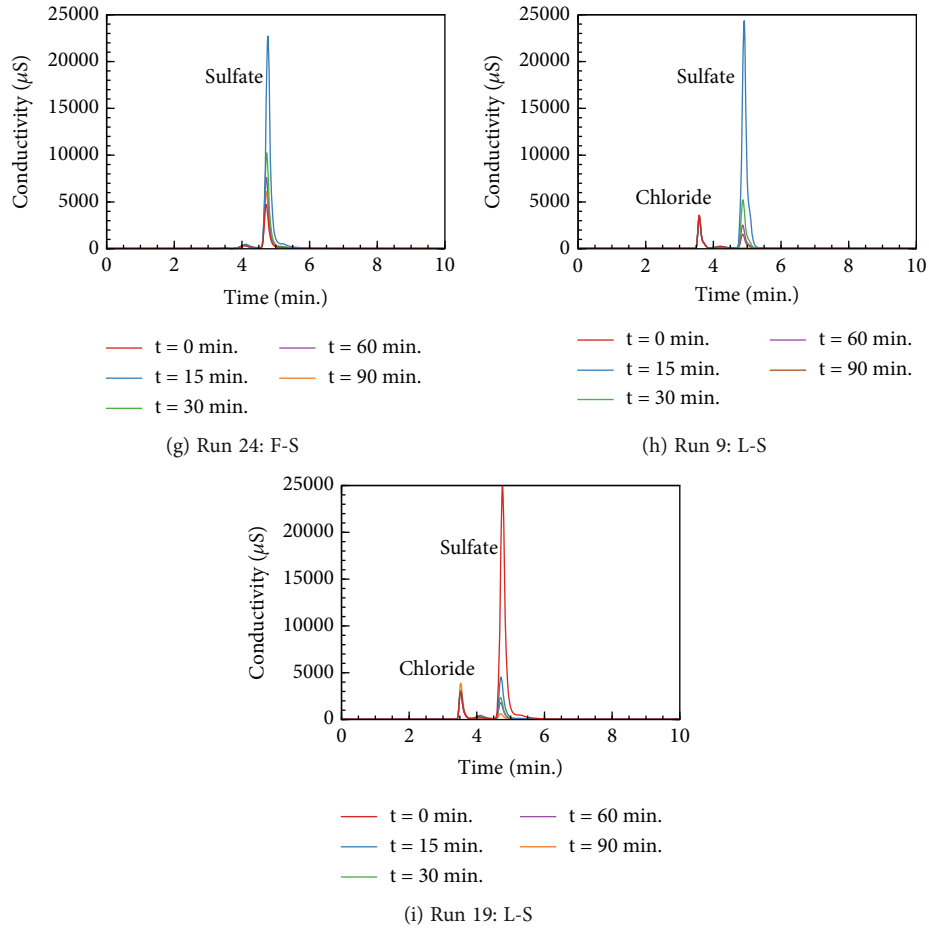


Figure 3: Comparison of the ion chromatographs for the MGS-1 standard experiments. Each row compares the spectra from a replicate experiment. Subtitle legend: C = coarse simulant exposed to solutions of W = water (no added salts), M = $MgSO_4$ solution, F = Fe(II)$SO_4$ solution, or L = LiCl solution. Note t0 is the solution control before exposure to the mineral simulant.

only the decrease in K was found to be statistically significant ($p = 0.03$). Exposure to LiCl significantly increased the Li intensity while decreasing the amount of K and Fe for MGS-1 coarse (Li: $p < 0.0001$; K: $p < 0.001$; and Fe: $p = 0.04$); Fe and K were also removed in the MGS-1 standard simulant (Li: $p < 0.0001$ and K: $p = 0.01$), whereas Al increased ($p = 0.03$).

*3.2.3. XRD and XRF Analysis.* XRD data of the starting simulants are reported in Figure S5 and show that the biggest difference in the mineralogy between the MGS-1 standard and coarse samples is the presence and absence of gypsum, respectively. XRD patterns were collected for the top of the packed bed from six selected sample runs (Samples W-C-T/B [2], M-C-T/B [3], L-C-T/B [8], W-S-T/B with water [5], M-S-T/B [7], and L-S-T/B). XRF was also obtained for the six samples. Overall, these results were consistent with the above observations from which techniques.

For the XRD, the results from the MGS-1 coarse and MGS-1 standard samples exposed to fluids were consistent, as expected. The major mineralogical differences in the diffraction patterns were in the clay content. Although specific clay mineral analysis was not performed (i.e., USGS clay mineral XRD procedures), there were clear changes in the ratios between the ~7 Å peak (likely dickite) and the ~10 Å peak (likely pyrophyllite) based on the JADE interpretation, which utilizes peak fitting, background subtraction, and profile matching to analyze diffraction patterns and estimate mineral proportion.

XRF data were collected to provide qualitative elemental analyses to aid mineralogical phase identification and also measure Fe and sulfur transport between samples and solution. All samples were observed to be high in Fe. The experimental ionic solution used in the weathering experiments had a minimal impact on the XRF analysis, as no significant trace of sulfur was detected in samples M-C-T/B (Run 3) and M-S-T/B (Run 7), although the sulfur measurements were slightly elevated above the $H_2O$ control tests. This result is consistent with $SO_4$ ions being dissolved, as opposed to precipitated.

## 4. Discussion

*4.1. Mars Simulant Alteration in Simulated Groundwater Flows.* Notable differences in the liquid chemistry of the outflow were observed between the MGS-1 standard and MGS-

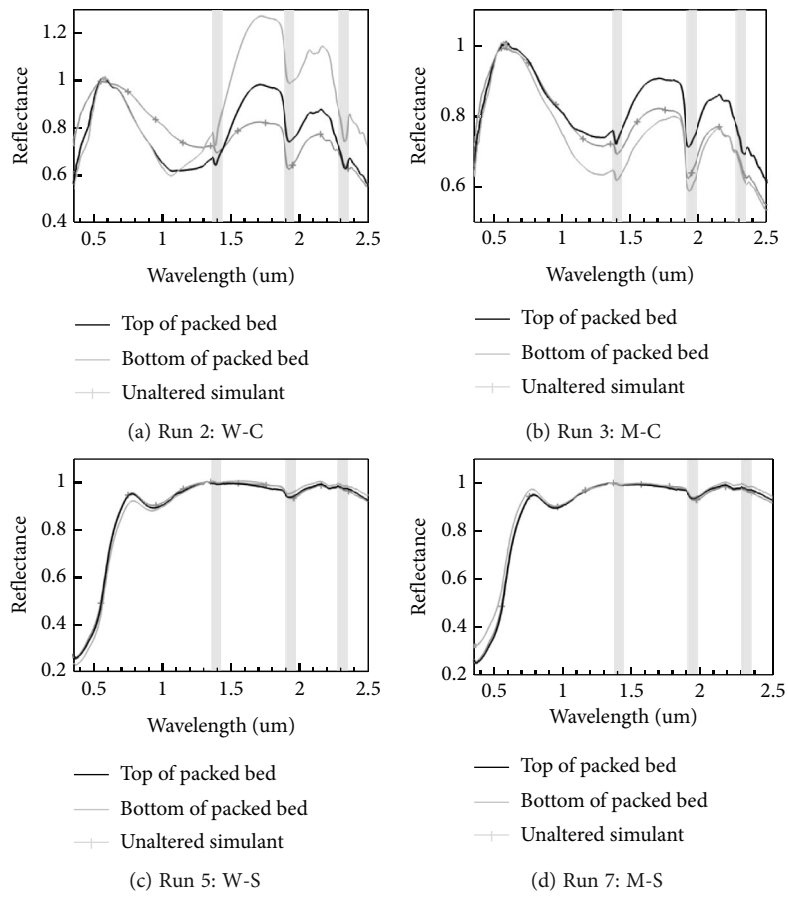


Figure 4: Vis-NIR reflectance spectra of dried simulant from four of the runs, to highlight the breadth of spectral features related to simulant and fluid choice. Additional spectra can be found in the Supporting Information.

1 coarse simulants (Figures 2 and 3). While the MGS-1 coarse appeared to undergo minimal changes, the MGS-1 standard lost sulfate throughout the continuous-flow experiments (Figure 6). This observation was supported by our IC analysis, which revealed a sulfate spike in all MGS-1 standard experiments located at 4.48 min (Figure S6). While all our MGS-1 standard experimental conditions demonstrated sulfate anions leaching into solution, experiments performed with MGS-1 coarse did not show the same weathering despite having a similar chemical composition to MGS-1 standard. Further, the data from MGS-1 coarse experiments only revealed anions expected from our flow through solutions (e.g., sulfate from $MgSO_4$ and $FeSO_4$ and chloride from LiCl salts), and the conductivity ($\mu$S) remained relatively constant between each sample, suggesting that there was not an additional source of sulfate in our samples (Figures S6–S13). However, in the MGS-1 standard, the sulfate spike appeared in all samples except our standard sample (controls), indicating that the material was easily solubilized during these experimental time scales. For experiments with the MGS-1 standard, the sulfate peak appeared immediately (e.g., within the first 15 min) for all conditions, including experiments performed without sulfate salts ($MgSO_4$ and $FeSO_4$), and there was more variation between the time-stamped liquid samples. Our experiments demonstrate a possible mechanism for how sulfate can be solubilized into solution and transported through sediments in a Martian subsurface. We attribute the difference between the two mineral analogs to the gypsum mineral ($CaSO_4 \bullet 2H_2O$) present in the MGS-1 standard, but absent in the MGS-1 coarse (see Figure S5). This suggests that sieving the MGS-1 standard in preference for larger grains (to produce MGS-1 coarse) selectively removed gypsum grains. Additionally, the smaller grain size of MGS-1 standard results in the materials having a larger surface area for which reactions can take place.

In experiments that contained LiCl as the flow-through solution, chloride was detected through our IC system at 3.52 min. In MSG-1 coarse experiments with LiCl (experiment L-C-T/B), there are minor peaks for Experiments 8 and 20 (Figure 2) related to our deionized water, as can be seen in $H_2O$-only experiments (W-C; Runs 2 and 10). The chloride peaks are also present at a significantly lower magnitude compared to the weathered sulfate peaks in MGS-1 (Figure 3, L-S; Runs 9, 12, and 19). These data suggest that, certainly, the source of sulfate in LiCl experiments is sourced from the simulated sediments.

Lastly, we investigated three flow rates (0.5, 1.0, and 2.0 mL/min) to understand the effect of flow on L-C experiments (Figure S23). The results revealed the presence of

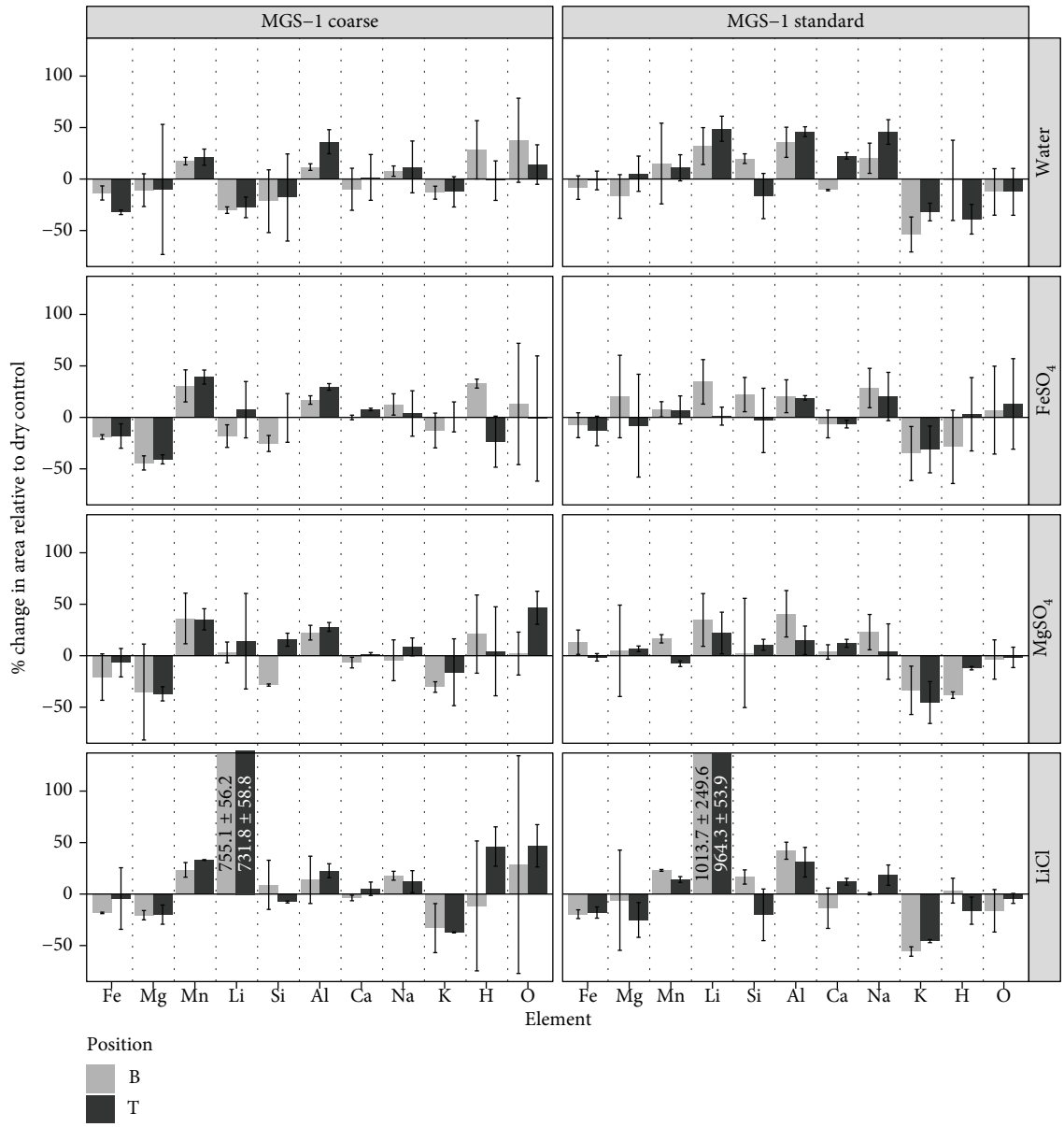


Figure 5: A comparison of the changes in elemental abundance between the unaltered simulant and the simulant exposed to various ionic solutions. The percent change reflects changes in the mean deconvolved areas for all elements except H and O; the percent (%) change for both elements was calculated from changes in their mean intensities. Note that the percent change for Li in the samples exposed to LiCl solutions was much greater than in all other conditions. To facilitate comparisons among different elements in other samples, the percent change for Li in the LiCl samples was truncated (the actual value ± standard deviation is written in the plotted bar). B, mineral from the bottom of the packed bed; T, mineral from the top of the packed bed.

chloride and artifacts related to our deionized water. The conductivity ($\mu$S) of the chloride was consistent between samples in lower flow rates (0.5 and 1.0 mL/min), while the fastest flow rate (2.0 mL/min) revealed a minor change. Additionally, the experiment performed at 2.0 mL/min only allowed for fewer time points as the fluid was injected rapidly through the system.

We observed changes in Vis-NIR spectral features between the approx. 8 cm of the top and bottom portions of the minerals utilized in the packed bed reactor during the experiment. In most cases, the bottom of the packed bed also had higher SINDEX values for most experiments, consistent with highly soluble sulfate being dissolved from the sediment by the water and mobilized. The exception in Runs 3 and 4 could be due to mineral heterogeneity or due to variable oxygen, which was not a controlled variable in these experiments.

In MGS-1 standard experiments with ionic solutions, the Vis-NIR continuum-removed metal–OH absorption (at 2.3 $\mu$m) was stronger at the bottom of the packed bed, which was exposed to fluid for longer in most experiments. This suggests enhanced formation or preservation of metal–OH-bearing phases where the simulant experienced longer fluid exposure. This spatial trend was seen in M-C (Runs 7 and 21), L-S (Run 19), and F-S (Runs 23 and 24) (Figure S24b,d).

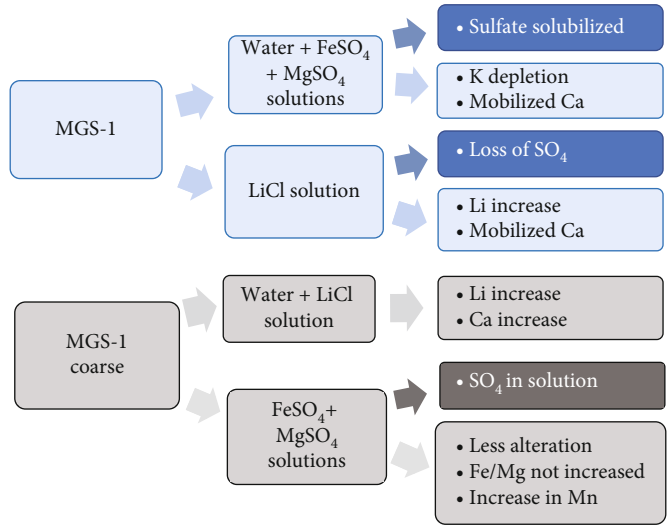


Figure 6: Flow chart summarizing the main experimental results from the three different simulants. The liquid analysis results are in a darker shade, and the solid analysis results are in a lighter shade.

In contrast, the 2.3 $\mu$m band depth was largely unchanged in the pure water experiments (Runs 5 and 13), indicating minimal alteration or metal–OH formation under these conditions. In addition to this adsorption band, SINDEX values were elevated at the top of the packed bed in W-S (Run 5 specifically) and F-S (Run 18 specifically). This pattern was opposite to that observed in the nonsulfate-containing experiments, likely reflecting the downward transport and accumulation of highly soluble sulfate species, potentially altering silicates in the upper column before being flushed out. Such sulfate mobilization, governed by gravitational flow and solubility gradients, appears to play a key role in modifying spectral signatures over depth. While these trends are broadly consistent across different ionic conditions, variability between runs, such as the magnitude and vertical distribution of spectral features, may reflect inherent heterogeneity in the mineralogical composition of the MGS-1 simulant.

The IC results indicate that exposure to water dissolved sulfate in the MGS-1 standard, but not the MGS-1 coarse simulant, indicating dissolution of a sulfate-containing mineral and possibly more loss of material in the MGS-1 standard simulant in comparison to the MGS-1 coarse material. Notably, the MGS-1 standard simulant contained $CaSO_4$ (likely in the form of anhydrite), reported as a major mineral component (the coarse simulant does not). Gypsum, the hydrated form of anhydrite, is readily soluble in water and could explain why the $SO_4$ peak was observed in the water exposed to the standard and not the coarse sediment. Dissolution of gypsum was further supported by Ca trends in the water-exposed samples relative to the dry control as observed by LIBS (Figure 5): Only the MGS-1 standard simulant experienced a significant change in the Ca levels, with Ca removed from the simulant material located at the bottom portion of the packed bed and elevated at the top of the packed bed, consistent with mobilized Ca from dissolved anhydrite being deposited at the top of the column. Indeed, our LIBS data indicates that water impacted the MGS-1 coarse simulant differently than the MGS-1 standard, suggesting that the mineralogy or amorphous content was impacted when the simulant was sieved for coarser grains.

In experiments with $SO_4^{-2}$ ions added to the solution, dissolution of gypsum may be inhibited in solutions containing $FeSO_4$ and $MgSO_4$, as the solution already contains sulfate. In our results, Ca did not change significantly in the experiments with either MGS-1 coarse (lacks gypsum) or MGS-1 standard (contains gypsum) exposed to $FeSO_4$ and $MgSO_4$ solutions (Figure 5). This assessment was further corroborated by the fact that in the control/unreacted MGS-1 standard sample, the mean Ca levels had the same trend exposed to LiCl solution as when exposed to water (with the bottom sediments being depleted relative to the dry control, while the top sediments were enriched in Ca; however, the changes in Ca in LiCl solutions were not found to be statistically significant). These results are also in agreement with Vis-NIR observations, which found that $FeSO_4$ and $MgSO_4$ solutions were not as efficient at mobilizing sulfate. Gypsum dissolution, in liberating Ca, may also partially explain the observed changes in K content. Notably, K was significantly more depleted in the MGS-1 standard sediments exposed to any aqueous fluids compared to the coarse samples. Moreover, this K depletion is more apparent in samples exposed to LiCl and water (given there is less experimental variation), with the bottom sediments in these packed beds being more depleted than the top sediments. This K depletion could be due to the influx of liberated Ca, which, having a similar atomic radius to K, could readily substitute for K. Ca, being double-charged, could have a significant impact on the geochemical properties and charge of the mineral. An additional consideration is the difference in reactive surface area between the two simulants, as the MGS-1 standard would have a much greater reactive surface area. K, as either a component of the glass or as a trace in the K-feldspar, has quite fast dissolution rates [57, 58]. This could also reprecipitate in the column throughout the experiment.

Notably, we observed Li even in samples that were not exposed to LiCl solutions (Figure 3). Our elemental analysis by XRF cannot detect Li; however, finding Li in the MGS-1 simulants is not surprising given that Li is commonly found in igneous rocks and minerals including basalt and olivine (typically in the 1–100 s ppm range), which make up ~27 and 14 wt% of the MGS-1 standard simulant [59, 60]; moreover, Li has been detected on Mars (ranging from < 15 ppm to local enrichments of ~60 ppm; [61]). Furthermore, it has been established in the literature that LIBS can detect Li in natural samples at these concentrations, including under Martian conditions, using the ChemCam LIBS instrument down to at least 3.2 ppm using the primary Li line at 670.8 nm [60, 61].

Our LIBS data suggests that Martian regolith transiently exposed to waters enriched in metals (e.g., Fe and Mg, up to 50 mM) may not retain (via sorption/precipitation/substitution) the passing metals. In particular, MGS-1 standard exposed to $FeSO_4$ and $MgSO_4$ solutions did not see an enhancement in the Fe or Mg signal via LIBS, respectively; in fact, for MGS-1 coarse sediments, the mean abundance of both of these metals significantly decreased when exposed to either $FeSO_4$ or $MgSO_4$ waters, which is expected as dissolution happens. In fact, for MGS-1 coarse, all solutions resulted in the loss of Fe to a similar degree, given the similar decrease in Fe intensity; Mg loss was only statistically significant in experiments exposed to either $FeSO_4$ or $MgSO_4$. Notably, we did not observe statistically significant changes in Fe or Mg in the MGS-1 standard when exposed to any solutions except LiCl. It is unclear why we observe more dissolution of these minerals in the MGS-1 coarse vs. the MGS-1 standard, given that the latter has a higher surface area for reactivity and would thus be expected to further promote dissolution. This suggests that changes in the Fe and Mg observed may be the result of differences in the simulants resulting from sieving preferentially removing certain materials. XRD shows that there is not a large difference in the mineralogical composition, with the only noted differences being that quartz and gypsum were not detected in the MGS-1 coarse but were in the standard, and $TiO_2$ was found in the coarse but not the standard. However, differences in these minerals do not explain the enhanced dissolution of Mg and Fe in the MGS-1 coarse simulant. Since XRD cannot capture the amorphous component, it may be possible that the two simulants differ more in this respect. The amorphous component, which would be more susceptible to dissolution, may be proportionally larger in the MGS-1 coarse simulant (though this remains to be tested). The amorphous content of MGS-1 (which should represent ~35 wt% of MGS-1 standard) is a combination of basaltic glass, opal, $MgSO_4$, ferrihydrite, and Fe-carbonate [29]. If there are more amorphous materials in MGS-1 coarse, then Fe loss may be enhanced due to relatively facile dissolution of ferrihydrite ($Fe^{3+}$) and Fe(II)carbonate, the former of which may rapidly dissolve even in $Fe(II)SO_4$ solution, given that it is reducing ($Fe^{2+}$) and acidic. $MgSO_4$ would also be expected to rapidly dissolve, though this should remove Mg in all the experiments and not just those with $MgSO_4$ and $FeSO_4$ solutions.

We observed Li in the MGS-1 standard and coarse simulants, indicating that Li was present in our samples prior to any experiments. Li is commonly found across a range of clay minerals on Earth, including sepiolite, illite, and smectites [62, 63]. During weathering, soluble Li released from primary minerals may be leached or reincorporated into secondary products like clays [64, 65]. This reincorporation occurs through several sorption mechanisms—adsorption onto mineral surfaces, absorption into the mineral lattice, and ion exchange at the surface—all broadly referred to as sorption [63, 66–68]. The small ionic radius of Li facilitates substitution for Mg or K, enhancing its compatibility with a variety of clay structures [34, 69]. As a result, Li is often enriched in the clay-sized fraction of sediments, particularly in trioctahedral smectites, which tend to host higher Li concentrations than dioctahedral smectites [64, 67]. Li sorption also correlates with grain size, as finer particles possess greater surface area and higher cation exchange capacity, promoting Li retention. Clay mineral grains < 2 $\mu$m in size, dominant in weathered and sedimentary settings, are especially effective Li hosts.

Samples exposed to LiCl solutions saw a significant boost in the Li intensity (+755%–1013% increase) in LIBS. These results indicate that Li content in Martian sediments can reflect enrichment from Li dissolved in passing fluids. Indeed, ChemCam has previously observed Li in Martian sediments [70], and it has been suggested that the Li could serve as a signal for enhanced clay content [35, 71]. In our experiments, we predict that the most likely process for Li enhancement is due to sorption. While the K signal decreased in these experiments, it did not appear significantly different when the simulants were exposed to LiCl compared to the other fluids; the loss in Mg was not statistically significant in either MGS-1 standard or coarse simulants (Figure 5). Alternatively, it is possible that the LiCl recrystallized out of solution as the solution dried onto the column at the end of the experiment. To facilitate hypothesis development regarding how the Li signal in sediments could change based on solution chemistry and mineralogy, future research should prioritize investigating the various mechanisms by which Li can be sorbed/precipitated/substituted onto Martian regolith.

Finally, of note is the increase in Mn content throughout all of the coarse samples exposed to any of the fluids tested. It is difficult to rationalize the increase in Mn content, sometimes in both the bottom and top of the MGS-1 coarse columns, given that Mn was not added to the solution to which the samples were exposed. One possibility is that aqueous alteration of the mineral modified the matrix so that it artificially enhanced the Mn LIBS signal due to matrix effects.

*4.2. Terrestrial Analogs of Mars.* Our results align with geologic systems where ionic solutions have a crucial impact on the weathering of basaltic terrains on Earth. Iceland, the Columbia River Basalt Group (CRBG, in the Pacific Northwest), and Hawaii are well-known areas of actively weathered basalt systems. In Iceland, weathered basalts from either rainfall infiltration or sulfate-rich geothermal fluids release and mobilize Ca, Mg, K, and Na [24, 72]. In these natural environments, the incongruent dissolution of

primary minerals results in the release of Fe, Ti, Al, and Si, which subsequently form secondary mineral phases, particularly under increasing pH, where clay minerals are synthesized [24, 72].

In the observations by [24], the sequential dissolution and oxidation of pyrite ($FeS_2$) increases the sulfate concentrations, while the dissolution of calcite increases the concentration of Ca [24]. Conversely, the dissolution of the basalt leads to the release of K, Fe, Mg, and Si, which are then adsorbed or form secondary mineral phases [24]. Additional studies report that under acidic conditions, K, Mg, Ca, and Na are highly mobile, and as the pH increases (> pH 5), these ions are incorporated into the secondary clay minerals and iron oxides [72]. In this second Earth-based system, reducing conditions at depth favor the presence of pyrite and begin to oxidize when exposed to $O_2$ (g) at shallower depths, which produces iron oxyhydroxides and sulfates [72].

In the CRBG, similar behavior is observed during basalt dissolution despite the lack of sulfate inputs. Specifically, Na and Ca are released and mobilized, while Fe, Mg, K, and Al are leached and later retained by secondary Fe and K phyllosilicates [23, 73]. In the Hawaiian basaltic system, Li is leached along with Mg, Ca, Na, and Fe and subsequently adsorbed onto secondary minerals formed from the leached ions, including kaolinite and Fe-oxides [26]. A second study of Li interactions in Hawaiian basaltic terrains found that weathering and release of Na, K, and Ca were highly efficient, while Li, Mg, Si, and Al were adsorbed or incorporated into secondary mineral surfaces [27]. These results are consistent with our experimental results, which show that certain ions are readily mobilized or can be retained in as adsorbed or incorporated into secondary minerals (e.g., sorbed Li) in Mars analog laboratory experiments and field studies. For example, we observed a decrease in K in experiments containing LiCl, while the detection of Li increased.

In addition to the field sites described above, models of the Martian basaltic weathering profiles formed by acidic sulfate–rich brines release and increase the concentration of Mg, Na, Ca, $SO_4$, and Cl with increasing depth [74]. In contrast, models using a neutral $MgSO_4$ solution project less basalt weathering, less secondary mineral formation, and lower mobility of ionic species compared to acidic sulfate models [74]. We observe a similar result in our study to these reported models, where dissolved sulfate increased in the lower region of the column. This result is notable, given that in natural systems such as those previously discussed, as well as in Craters of the Moon National Monument, Idaho, secondary Na-sulfate minerals have been observed near the surface, formed from basalt weathered by sulfate-rich brines and subsequent evaporation [75]. Secondary mineral phases of weathered synthetic basalts have been identified by experimental approaches by [76]. These secondary phases are a result of acid sulfate weathering, which produced secondary phases including Mg, Fe, Ca, and Al sulfates, amorphous silica, and ferric oxides; the predominant phases under different conditions are amorphous $SiO_2$, gypsum, $FeSO_4 \bullet nH_2O$, Fe oxide (goethite), and others [76]. Links between Iceland, Hawaii, and the basaltic region of the Pacific Northwest (CRBG and Craters of the Moon National Monument) and Mars have been made in terms of basalt sulfate weathering and secondary mineral formation from leached ions. Our results have implications for how sulfate and other ions move vertically through the sediment column, given that environmental conditions (fluid composition, pH, temperature, and redox activity) can lead to different mineral formation, such as gypsum and anhydrite [76, 77].

*4.3. Mission Relevance.* While our work is not directly related to any mission data, the simulant and techniques utilized are comparable to ongoing missions. The MGS-1 standard and coarse simulants that were successfully used in this work are mineralogical standards that were designed to replicate the windblown soil Rocknest deposits at Gale Crater (the MSL Curiosity landing site); the MGS-1 design was informed by ChemMin XRD data to estimate the crystalline fraction, along with geochemical constraints to estimate the amorphous fraction [29]. As we are using relevant mineral analogs, the results from our simulated groundwater alteration study and future studies using MGS-1 could be particularly applicable to future mission data from MSL: in particular, the elemental abundances we observed using LIBS which were obvious indicators of mineral alteration upon exposure to groundwaters of different composition, which can be related to other experimental and modelled works within the field. Relevant to Perseverance, XRF can also be compared to PIXL and Vis-NIR, and LIBS can be analogous to components of SuperCam. Additionally, this work is relevant to ESA's ExoMars rover [1], which will be equipped with a deep drill that will inform geologic history.

There are some notable differences between the ChemCam and SuperCam LIBS on the Curiosity and Perseverance rovers, respectively, and the laboratory LIBS at JPL that was used in this study that should be considered when comparing experiments like this to mission data (see Figure 7). LIBS peaks are known for having intensities that can vary significantly from shot to shot or point to point on a single pellet, with some elements showing greater variability than others [78]. This variability can hinder LIBS' ability to distinguish between slight changes in elemental abundance between samples. The quality of a LIBS spectrum, and thus the intensity of emission lines, is also dependent on how well the laser couples with the sample, in addition to the laser pulse energy. For ChemCam/SuperCam on MSL, the LIBS instrument is typically operated using ~14 mJ laser pulses [78], which is much higher than our JPL LIBS instrument that operates at ~0.8 mJ. Additionally, the JPL LIBS cannot acquire spectra below ~390 nm (whereas ChemCam/SuperCam can go down to 240 nm); this restricts the emission lines that can be used in this study. Notably, it was found that for ChemCam, some elements were best quantified using their UV emission lines as these experienced relatively minimal shot-to-shot variations (e.g., Si [288.2 nm], Al [307.5 and 308.9 nm], Fe [260 nm], and Ti [425.5 nm]; [78]). Finally, unlike ChemCam/SuperCam, which acquires a spectrum per shot, the JPL LIBS acquires a single, average spectrum of all shots acquired per point (i.e., in this work, an average spectrum from 250 shots). Overall, the lower LIBS

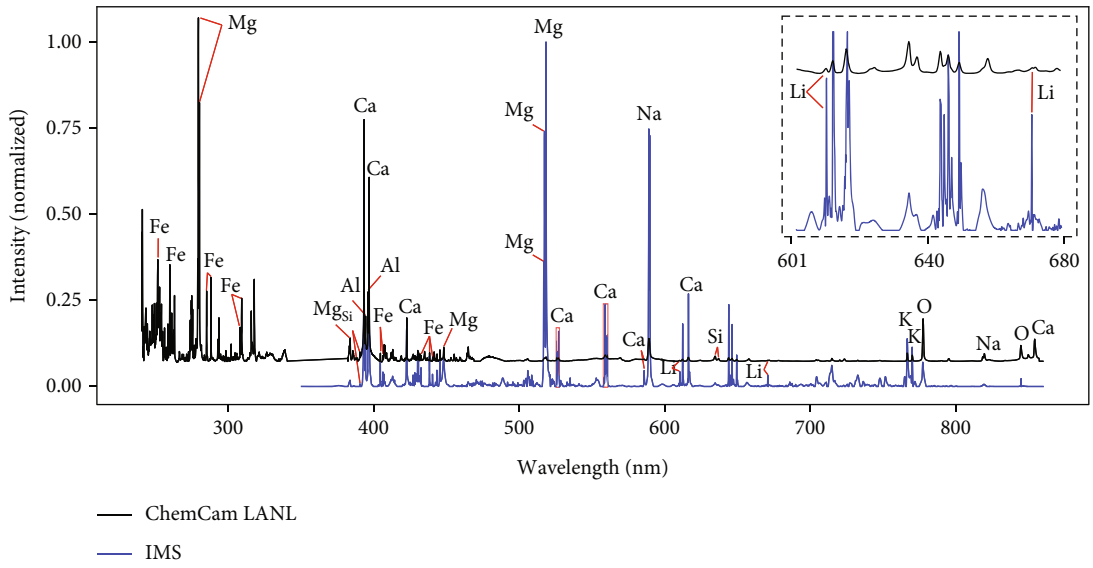


FIGURE 7: LIBS comparison of MGS-1 standard simulant as measured by the ChemCam engineering equivalent at Los Alamos National Laboratory (black) and the JPL Impossible Sensing (IMS) LIBS instrument used in this study (blue). Note that the ChemCam instrument can measure further into the UV by comparison. The ChemCam spectrum is an average of 30 spectra of a total of 30 shots each (one spectrum per shot), whereas the IMS spectrum is the mean from 13 spectra, each an average of 250 shots. The inset in the top right corner shows the region from 601 to 680 nm and highlights the two Li emission lines detected in this work. Notably, the emission lines were detected by both instruments but are significantly more pronounced for the IMS system.

power of the JPL LIBS generates a weaker signal compared to ChemCam when the same number of shots is used; consequently, the JPL instrument did not couple as readily with either of the Martian simulants. Increasing the number of shots from 30 to 250 boosted the signal-to-noise ratio significantly, but increasing the number of shots past 250 did not have a significant effect. As each LIBS spectrum represents the average of 250 shots, increasing the number of shots from 30 (used by ChemCam) to 250 also increases point-to-point variability as it leads to a decrease in the peak intensity for some elements (e.g., H, O, and Si) and an increase in the background continuum [51]. As Figure 7 shows, the JPL LIBS instrument was capable of producing spectra with intense peaks of interest when 250 shots were used (vs. the mean spectrum stemming from 30 spectra collected from 30 shots from ChemCam).

Due to the nature of the JPL LIBS instrument vs. ChemCam/SuperCam, the elemental intensities derived from the JPL LIBS will have more variance than those from ChemCam/SuperCam, especially for H, O, and Si. Indeed, as seen in Figure 5, the variation in Si, H, and O contents between experimental replicates relative to the dry simulant is large, hindering any attempts to discern whether any of the ionic solutions had a significant impact on these elements. ANOVA testing showed no statistically significant difference in Si, H, or O content between samples exposed to the different ionic solutions. Additionally, there is significant variation in the Fe and Mg content of replicates in all but two of the samples. This variation could be due to the fact that the Fe line used is a relatively weaker emission line (432.6 nm) compared to those for Fe in the UV. For Mg, the line used was typically the most intense peak in the LIBS spectra (518.3 nm); thus, the variation may be due to self-absorption of the signal, an effect that commonly occurs in the more intense LIBS signals, worsening as the element increases in abundance [79].

LIBS can thus be applied productively in laboratory Mars mineral weathering experiments like those described here, and further investigations of this type can help improve our understanding of Martian materials analyzed by ChemCam and SuperCam. However, to draw inferences from experimental data to observations on Mars, it is important to take into consideration the differences between the LIBS instrument used and ChemCam or SuperCam when conducting analog studies, which is true for all analog instruments. Overall, we would expect both ChemCam and SuperCam to be capable of detecting the changes seen in our experiments (e.g., see Figure 7) as well as even more subtle differences given its higher power, less variability, and access to the UV region (< 390 nm) which has more intense and stable Fe, Si, Mg, Al, and Ti peaks. Although the JPL LIBS was more sensitive toward Li compared to ChemCam (Figure Figure 7), we predict that our Li results are still relevant to ChemCam, given that it was still capable of picking up both Li peaks in the MGS-1 sample (670.8 and 610.4 nm; although the peaks were very weak). Moreover, ChemCam has previously detected Li on Mars, and laboratory experiments on Earth have shown the instrument capable of detecting Li down to at least 3.2 ppm levels [61]. Finally, as shown in our experiments, a passing 50 mM solution of LiCl has a significant impact on the Li present and detectable by LIBS.

The XRF used in this study was performed on bulk powders and is thus relatively limited when compared to PIXL, which is a micro-XRF and shows elemental maps of the areas it scans on a micron scale resolution [80]. The XRF data from this study indicated that $SO_4$ ions were being

dissolved, as opposed to precipitated. While in our experiments, the fluid flow is a known component, if these data were coupled with in situ measurements on Mars, they could allow researchers to reconstruct palaeogroundwater flows.

*4.4. Use of Continuous-Flow Reactors for Martian Mineral Studies.* Clogging the reactor is a common problem in flow chemistry [15]. However, MGS-1 standard and MGS-1 coarse gave successful results. As a lesson from this work, clay material and other fine materials may also be challenging in this system, and a continuous-flow experiment protocol would require significant optimization. However, changing the reactive surfaces would impact the results as well. For the present study, variations in reaction time and flow rate were initially tested and found to be viable under the conditions explored.

Within packed bed and continuous-flow studies, there is a variety of parameters to explore. Herein, we focused on simulated groundwater composition, mineral simulant, and flow rate. Future studies should expand on this work, including exploring mineral components and more complex ionic solutions and simulated Martian groundwater (including Si). These types of continuous flow reactors are especially beneficial for handling and generating hazardous materials [81]. Therefore, testing very active redox materials could benefit from such a system. In addition, continuous-flow systems are useful for experiments with varying temperature [15] as well as for photochemical experiments [82–84], which would be important parameters to test for the Martian surface. In addition, packed beds can be telescoped [85] together to test more complex setups (e.g., mixtures of clay material, organic species, and inorganic additives). Clay materials can also be efficient with a dialysis membrane in order to avoid clogging [86]. Temperature and photochemical environment could then be varied across the packed beds in order to simulate different layers of Martian sediment. In situ monitoring can be done in line, but it would be challenging to monitor something such as pH, spectroscopy of the packed bed, or ionic composition of the fluid throughout the experiment in situ. A future direction of this work could also include kinetic measurements to better understand timescale limitations of the instruments utilized.

*4.5. Astrobiological Relevance.* Understanding the presence of liquid water, as well as its geochemical characteristics, is important for understanding the habitability of a given environment and constraining what kind of chemistry or biology could be possible [87]. Understanding the redox conditions of an environment is one such parameter. In the case of MGS-1 coarse, the anions in the solution did not change substantially throughout the experiment, which would mean that the geochemistry of the liquid was more closely preserved (at least in the case of anions). However, the release of $SO_4$ ion in the case of MGS-1 standard would impact the surrounding water and change the redox potential and possible chemical reactions/metabolic pathways that could occur within the resulting solution. This could be particularly relevant to potential metabolic processes, as there are multiple sulfur-relevant metabolic pathways, including sulfate reducers that are explored in astrobiology (e.g., [88–90]).

Notably, on Mars' surface in the present day, pure liquid water and elevated temperatures are not expected. Some researchers have postulated that microscopic liquid water at subzero temperatures may still have important reactions, including sulfate formation [91]. Varying the temperature and scale could be a viable future direction for this work. Additionally, understanding the presentence and reaction of organic material is a research component of astrobiology and future research on Mars (e.g., [92]). Future work could integrate biologically relevant organic molecules to understand how they interact with the simulant, as well as whether there are any organic reactions that occur under the reaction conditions.

## 5. Conclusions

Here, we explored the aqueous alteration of two Martian soil simulants (MGS-1 coarse and MGS-1 standard) with simulated Martian groundwaters in a novel continuous-flow setup. However, both MGS-1 simulants were successful in reacting with simulated Mars groundwater solutions. We observed an impact on both the liquid and solid components of this reaction due to aqueous mineral reactions over the duration of the flow experiment. Overall, the liquid samples for MGS-1 standard showed large sulfate peaks indicating sulfate mineral dissolution, whereas liquid samples for MGS-1 coarse primarily contained the ions from salts used in the groundwater simulant (i.e., mineral dissolution was not observed). This discrepancy was likely due to the removal of gypsum when MGS-1 was sieved for larger grain sizes to make the MGS-1 coarse simulant. Many different forms of hydrated sulfates have been detected on Mars, several ongoing Mars missions have identified sulfate in association with aqueous alteration, and this study provides support that this alteration can occur on a relatively rapid timeline. This study is additionally in line with known terrestrial geologic systems with sulfate weathering. Changes in the Vis-NIR were primarily attributed to mineral dissolution, and LIBS was useful in measuring elemental abundances indicative of groundwater/mineral interaction. These data can be used to better understand mission results on Mars—including constraining how we look for clay materials and constraining sulfate leaching. Lithium was either precipitated or sorbed by these mineral simulants and could be used as an indicator that clays are present or, as shown here, that Li-rich fluids have passed through. The clay contents provide information on past liquid water interactions with regolith, which is relevant for astrobiology since clays have high organic preservation potential. In the Fe/Mg sulfate groundwater experiments, there was less alteration of the MGS-1 standard simulant, which may better represent the average grain size of Martian sediments vs. MGS-1 coarse, than in other liquid phases (e.g., water or LiCl). Thus, sediments in areas that would have experienced higher loads of Fe or Mg in sulfate-rich groundwater could be more pristine.

## Data Availability Statement

The data that support the findings of this study are openly available in the JPL Open Repository at 10.48577/jpl .VODOCB.

## Conflicts of Interest

The authors declare no conflicts of interest.

## Funding

This study was funded by the JPL Spontaneous Research and Technology Development (RTD) award "Novel Continuous Flow Reaction Design to Test Martian Weathering" and the National Aeronautics and Space Administration Habitable Worlds Grant "Feeding Enceladus' Deep Biosphere."

## Acknowledgments

The research was carried out at the Jet Propulsion Laboratory, California Institute of Technology, under a contract with the National Aeronautics and Space Administration (80NM0018D0004), 2024. All rights reserved. We thank Ronald K. Martinez, Dorothea Delapp, Nina Lanza, and Samuel Clegg for the spectrum of the MGS-1 simulant acquired by the ChemCam engineering model at Los Alamos National Laboratory as part of the work under LER's Mars Science Laboratory (MSL) participating scientist (PS) grant.

## Supporting Information

Additional supporting information can be found online in the Supporting Information section. *(Supporting Information)* The Supporting Information (SI) file contains reaction images (Figures S1–S4), a table of all experiments ran (Table S1), simulant standards (Figure S5), data and spectra from the IC (Section III, Figures S6–S23), Vis-NIR (Figures S24–S29), XRF (Figure S32), LIBS (Table S2, Figures S33–S38), and XRD images and patterns (Figures S30 and S31). The data is openly available in a public repository that issues datasets.

## References

[1] A. Kereszturi, B. Bradák, E. Chatzitheodoridis, and G. Ujvari, "Indicators and Methods to Understand Past Environments From ExoMars Rover Drills," *Origins of Life and Evolution of Biospheres* 46, no. 4 (2016): 435–454, https://doi.org/10.1007/s11084-016-9492-3.

[2] M. A. Chan, B. Beitler, W. T. Parry, J. Ormö, and G. Komatsu, "A Possible Terrestrial Analogue for Haematite Concretions on Mars," *Nature* 429, no. 6993 (2004): 731–734, https://doi.org/10.1038/nature02600.

[3] J. Frydenvang, P. J. Gasda, J. A. Hurowitz, et al., "Diagenetic Silica Enrichment and Late-Stage Groundwater Activity in Gale Crater," *Mars. Geophysical Research Letters* 44, no. 10 (2017): 4716–4724.

[4] J. P. Grotzinger, R. E. Arvidson, J. F. Bell Iii, et al., "Stratigraphy and Sedimentology of a Dry to Wet Eolian Depositional System, Burns Formation, Meridiani Planum, Mars," *Earth and Planetary Science Letters* 240, no. 1 (2005): 11–72, https://doi.org/10.1016/j.epsl.2005.09.039.

[5] J. A. Hurowitz and W. W. Fischer, "Contrasting Styles of Water–Rock Interaction at the Mars Exploration Rover Landing Sites," *Geochimica et Cosmochimica Acta* 127 (2014): 25–38, https://doi.org/10.1016/j.gca.2013.11.021.

[6] S. W. Squyres, R. E. Arvidson, J. F. Bell III, et al., "The Spirit Rover's Athena Science Investigation at Gusev Crater, Mars," *Science* 305, no. 5685 (2004): 794–799, https://doi.org/10.1126/science.3050794.

[7] V. Z. Sun, K. M. Stack, L. C. Kah, et al., "Late-Stage Diagenetic Concretions in the Murray Formation, Gale Crater, Mars," *Icarus* 321 (2019): 866–890, https://doi.org/10.1016/j.icarus.2018.12.030.

[8] R. E. Kronyak, L. C. Kah, K. S. Edgett, et al., "Mineral-Filled Fractures as Indicators of Multigenerational Fluid Flow in the Pahrump Hills Member of the Murray Formation, Gale Crater, Mars," *Earth and Space Science* 6, no. 2 (2019): 238–265, https://doi.org/10.1029/2018EA000482.

[9] S. Sharma, R. D. Roppel, A. E. Murphy, et al., "Diverse Organic-Mineral Associations in Jezero Crater, Mars," *Nature* 619, no. 7971 (2023): 724–732, https://doi.org/10.1038/s41586-023-06143-z.

[10] M. Nachon, G. López-Reyes, P.-Y. Meslin, et al., "Light-Toned Veins and Material in Jezero Crater, Mars, as seen In-Situ via NASA's Perseverance Rover (Mars 2020 Mission): Stratigraphic Distribution and Compositional Results from the Supercam Instrument," in *Proceedings of the 54th Lunar and Planetary Science Conference 2023* (Lunar and Planetary Institute, 2023), 2673.

[11] S. W. Squyres, A. H. Knoll, R. E. Arvidson, et al., "Two Years at Meridiani Planum: Results From the Opportunity Rover," *Science* 313, no. 5792 (2006): 1403–1407, https://doi.org/10.1126/science.1130890.

[12] B. L. Ehlmann, J. F. Mustard, S. L. Murchie, et al., "Subsurface Water and Clay Mineral Formation During the Early History of Mars," *Nature* 479, no. 7371 (2011): 53–60, https://doi.org/10.1038/nature10582.

[13] J. R. Michalski, J. Cuadros, P. B. Niles, J. Parnell, A. Deanne Rogers, and S. P. Wright, "Groundwater Activity on Mars and Implications for a Deep Biosphere," *Nature Geoscience* 6, no. 2 (2013): 133–138, https://doi.org/10.1038/ngeo1706.

[14] S. G. Newman and K. F. Jensen, "The Role of Flow in Green Chemistry and Engineering," *Green Chemistry* 15 (2013): 1456–1472, https://doi.org/10.1039/C3GC40374B.

[15] M. B. Plutschack, B. Pieber, K. Gilmore, and P. H. Seeberger, "The Hitchhiker's Guide to Flow Chemistry," *Chemical Reviews* 117, no. 18 (2017): 11796–11893, https://doi.org/10.1021/acs.chemrev.7b00183.

[16] E. M. Dixon, A. S. Elwood Madden, E. M. Hausrath, and M. E. Elwood Madden, "Assessing Hydrodynamic Effects on Jarosite Dissolution Rates, Reaction Products, and Preservation on Mars," *Journal of Geophysical Research: Planets* 120, no. 4 (2015): 625–642, https://doi.org/10.1002/2014JE004779.

[17] S. R. Gainey, E. M. Hausrath, J. A. Hurowitz, and R. E. Milliken, "Nontronite Dissolution Rates and Implications for Mars," *Geochimica et Cosmochimica Acta* 126 (2014): 192–211, https://doi.org/10.1016/j.gca.2013.10.055.

[18] J. A. Hurowitz, S. M. McLennan, N. J. Tosca, et al., "In Situ and Experimental Evidence for Acidic Weathering of Rocks

and Soils on Mars," *Journal of Geophysical Research: Planets* 111, no. E2 (2006): E02S19, https://doi.org/10.1029/2005JE002515.

[19] J. A. Hurowitz, S. M. McLennan, D. H. Lindsley, and M. A. A. Schoonen, "Experimental Epithermal Alteration of Synthetic Los Angeles Meteorite: Implications for the Origin of Martian Soils and Identification of Hydrothermal Sites on Mars," *Journal of Geophysical Research* 110, no. E7 (2005): E07002, https://doi.org/10.1029/2004JE002391.

[20] J. C. Viennet, B. Bultel, and S. C. Werner, "Experimental Reproduction of the Martian Weathering Profiles Argues for a Dense Noachian CO2 Atmosphere," *Chemical Geology* 525 (2019): 82–95, https://doi.org/10.1016/j.chemgeo.2019.07.009.

[21] M. E. Elwood Madden, A. S. Madden, and J. D. Rimstidt, "Applying a Jarosite Stopwatch to Determine the Duration of Aqueous Diagenesis," *Geology* 37, no. 7 (2009): 635–638.

[22] B. N. Pritchett, M. E. Elwood Madden, and A. S. Madden, "Jarosite Dissolution Rates and Maximum Lifetimes in High Salinity Brines: Implications for Earth and Mars," *Earth and Planetary Science Letters* 357–358 (2012): 327–336.

[23] L. L. Baker and O. K. Neill, "Geochemistry and Mineralogy of a Saprolite Developed on Columbia River Basalt: Secondary Clay Formation, Element Leaching, and Mass Balance During Weathering," *American Mineralogist* 102, no. 8 (2017): 1632–1645.

[24] T. L. Cole, M. A. Torres, and P. C. Kemeny, "The Hydrochemical Signature of Incongruent Weathering in Iceland," *Journal of Geophysical Research: Earth Surface* 127, no. 6 (2022): e2021JF006450.

[25] E. C. Marcucci and B. M. Hynek, "Laboratory Simulations of Acid-Sulfate Weathering Under Volcanic Hydrothermal Conditions: Implications for Early Mars," *Journal of Geophysical Research: Planets* 119, no. 3 (2014): 679–703.

[26] J.-S. Ryu, N. Vigier, S.-W. Lee, K.-S. Lee, and O. A. Chadwick, "Variation of Lithium Isotope Geochemistry during Basalt Weathering and Secondary Mineral Transformations in Hawaii," *Geochimica et Cosmochimica Acta* 145 (2014): 103–115, https://doi.org/10.1016/j.gca.2014.08.030.

[27] Y. Huh, L. H. Chan, and O. A. Chadwick, "Behavior of Lithium and Its Isotopes During Weathering of Hawaiian Basalt," *Geochemistry, Geophysics, Geosystems* 5, no. 9 (2004): https://doi.org/10.1029/2004GC000729.

[28] D. L. Bish, D. F. Blake, D. T. Vaniman, et al., "X-Ray Diffraction Results From Mars Science Laboratory: Mineralogy of Rocknest at Gale Crater," *Science* 341, no. 6153 (2013): 1238932, https://doi.org/10.1126/science.1238932.

[29] K. M. Cannon, D. T. Britt, T. M. Smith, R. F. Fritsche, and D. Batcheldor, "Mars Global Simulant MGS-1: A Rocknest-Based Open Standard for Basaltic Martian Regolith Simulants," *Icarus* 317 (2019): 470–478, https://doi.org/10.1016/j.icarus.2018.08.019.

[30] G. H. Peters, W. Abbey, G. H. Bearman, et al., "Mojave Mars Simulant—Characterization of a New Geologic Mars Analog," *Icarus* 197, no. 2 (2008): 470–479, https://doi.org/10.1016/j.icarus.2008.05.004.

[31] F. Rivera-Hernández, D. Y. Sumner, N. Mangold, et al., "Grain Size Variations in the Murray Formation: Stratigraphic Evidence for Changing Depositional Environments in Gale Crater, Mars," *Journal of Geophysical Research: Planets* 125, no. 2 (2020): e2019JE006230, https://doi.org/10.1029/2019JE006230.

[32] D. C. Catling, "A Chemical Model for Evaporites on Early Mars: Possible Sedimentary Tracers of the Early Climate and Implications for Exploration," *Journal of Geophysical Research: Planets* 104, no. E7 (1999): 16453–16469.

[33] S. P. Schwenzer, J. C. Bridges, R. C. Wiens, P. G. Conrad, S. P. Kelley, R. Leveille, et al., "Fluids During Diagenesis and Sulfate Vein Formation in Sediments at Gale Crater, Mars," *Meteoritics & Planetary Science* 51, no. 11 (2016): 2175–2202, https://doi.org/10.1111/maps.12668.

[34] E. Dehouck, A. Cousin, N. Mangold, et al., "Bedrock Geochemistry and Alteration History of the Clay-Bearing Glen Torridon Region of Gale Crater, Mars," *Journal of Geophysical Research: Planets* 127, no. 12 (2022): e2021JE007103, https://doi.org/10.1029/2021JE007103.

[35] J. Frydenvang, N. Mangold, R. C. Wiens, et al., "The Chemostratigraphy of the Murray Formation and Role of Diagenesis at Vera Rubin Ridge in Gale Crater, Mars, as Observed by the ChemCam Instrument," *Journal of Geophysical Research: Planets* 125, no. 9 (2020): e2019JE006320, https://doi.org/10.1029/2019JE006320.

[36] N. Noda, Y. Sekine, S. Tan, et al., "Characterization of Groundwater Chemistry Beneath Gale Crater on Early Mars by Hydrothermal Experiments," *Icarus* 386 (2022): 115149, https://doi.org/10.1016/j.icarus.2022.115149.

[37] E. S. Kite, I. Halevy, M. A. Kahre, M. J. Wolff, and M. Manga, "Seasonal Melting and the Formation of Sedimentary Rocks on Mars, With Predictions for the Gale Crater Mound," *Icarus* 223, no. 1 (2013): 181–210, https://doi.org/10.1016/j.icarus.2012.11.034.

[38] E. B. Rampe, D. F. Blake, T. F. Bristow, et al., "Mineralogy and Geochemistry of Sedimentary Rocks and Eolian Sediments in Gale Crater, Mars: A Review After Six Earth Years of Exploration With Curiosity," *Geochemistry* 80, no. 2 (2020): 125605, https://doi.org/10.1016/j.chemer.2020.125605.

[39] H. B. Franz, A. C. McAdam, D. W. Ming, et al., "Large Sulfur Isotope Fractionations in Martian Sediments at Gale Crater," *Nature Geoscience* 10, no. 9 (2017): 658–662, https://doi.org/10.1038/ngeo3002.

[40] J. P. Grotzinger, J. Crisp, A. R. Vasavada, et al., "Mars Science Laboratory Mission and Science Investigation," *Space Science Reviews* 170 (2012): 5–56, https://doi.org/10.1007/s11214-012-9892-2.

[41] E. B. Rampe, T. F. Bristow, R. V. Morris, et al., "Mineralogy of Vera Rubin Ridge From the Mars Science Laboratory CheMin Instrument," *Journal of Geophysical Research: Planets* 125, no. 9 (2020): e2019JE006306, https://doi.org/10.1029/2019JE006306.

[42] R. Y. Sheppard, R. E. Milliken, M. Parente, and Y. Itoh, "Updated Perspectives and Hypotheses on the Mineralogy of Lower Mt. Sharp, Mars, as Seen From Orbit," *Journal of Geophysical Research: Planets* 126, no. 2 (2021): e2020JE006372, https://doi.org/10.1029/2020JE006372.

[43] J. L. Eigenbrode, R. E. Summons, A. Steele, et al., "Organic Matter Preserved in 3-Billion-Year-Old Mudstones at Gale Crater, Mars," *Science* 360, no. 6393 (2018): 1096–1101, https://doi.org/10.1126/science.aas9185.

[44] J. P. Grotzinger, D. Y. Sumner, L. C. Kah, et al., "A Habitable Fluvio-Lacustrine Environment at Yellowknife Bay, Gale Crater, Mars," *Science* 343, no. 6169 (2014): 1242777.

[45] M. Millan, A. J. Williams, A. C. Mcadam, et al., "Sedimentary Organics in Glen Torridon, Gale Crater, Mars: Results from the SAM Instrument Suite and Supporting Laboratory

Analyses," *Journal of Geophysical Research: Planets* 127, no. 11 (2022): e2021JE007107, https://doi.org/10.1029/2021JE007107.

[46] W. Constantine and D. Percival, "Wavelet Methods for Time Series Analysis," 2017.

[47] D. B. Percival and A. T. Walden, *Wavelet Methods for Time Series Analysis* 4, Cambridge University Press, 2017).

[48] K. H. Liland, T. Almøy, and B. Mevik, "Optimal Choice of Baseline Correction for Multivariate Calibration of Spectra," *Applied Spectroscopy* 64, no. 9 (2010): 1007–1016, https://doi.org/10.1366/000370210792434350.

[49] M. A. D. M. Franco, D. M. B. P. Milori, and P. R. V. Boas, "Comparison of Algorithms for Baseline Correction of LIBS Spectra for Quantifying Total Carbon in Brazilian Soils" 2018, https://arxiv.org/abs/1805.03695.

[50] T. V. Elzhov, K. M. Mullen, A. Spiess, and B. Bolker, "minpack.lm: R Interface to the Levenberg-Marquardt Nonlinear Least-Squares Algorithm Found in MINPACK, Plus Support for Bounds" 2023, R package version 1.2-4, https://CRAN.R-project.org/package=minpack.lm.

[51] N. H. Thomas, B. L. Ehlmann, D. E. Anderson, et al., "Characterization of Hydrogen in Basaltic Materials With Laser-Induced Breakdown Spectroscopy (LIBS) for Application to MSL ChemCam Data," *Journal of Geophysical Research: Planets* 123, no. 8 (2018): 1996–2021, https://doi.org/10.1029/2017JE005467.

[52] R. Lenth, "Emmeans: Estimated Marginal Means, aka Least-Squares Means" 2020, R Package Version 1.4.8. https://CRAN.Rproject.org/package=emmeans.

[53] R. N. Clark and T. L. Roush, "Reflectance Spectroscopy: Quantitative Analysis Techniques for Remote Sensing Applications," *Journal of Geophysical Research* 89, no. 7 (1984): 6329–6340.

[54] C. E. Viviano, F. P. Seelos, S. L. Murchie, et al., "Revised CRISM Spectral Parameters and Summary Products Based on the Currently Detected Mineral Diversity on Mars," *Journal of Geophysical Research: Planets* 119, no. 6 (2014): 1403–1431, https://doi.org/10.1002/2014JE004627.

[55] R. N. Clark, T. V. V. King, M. Klejwa, G. A. Swayze, and N. Vergo, "High Spectral Resolution Reflectance Spectroscopy of Minerals," *Journal of Geophysical Research: Solid Earth* 95, no. B8 (1990): 12653–12680.

[56] A. Gendrin, N. Mangold, J. P. Bibring, Y. Langevin, B. Gondet, F. Poulet, et al., "Sulfates in Martian Layered Terrains: The OMEGA/Mars Express View," *Science* 307, no. 5715 (2005): 1587–1591, https://doi.org/10.1126/science.1109087.

[57] J. L. Palandri and Y. K. Kharaka, *A Compilation of Rate Parameters of Water-Mineral Interaction Kinetics for Application to Geochemical Modeling (No. 2004-1068)* (US Geological Survey, 2004), https://pubs.usgs.gov/of/2004/1068/.

[58] M. Heřmanská, M. J. Voigt, C. Marieni, J. Declercq, and E. H. Oelkers, "A Comprehensive and Consistent Mineral Dissolution Rate Database: Part II: Secondary Silicate Minerals," *Chemical Geology* 636 (2023): 121632, https://doi.org/10.1016/j.chemgeo.2023.121632.

[59] L.-H. Chan, J. C. Alt, and D. A. H. Teagle, "Lithium and Lithium Isotope Profiles Through the Upper Oceanic Crust: A Study of Seawater–Basalt Exchange at ODP Sites 504B and 896A," *Earth and Planetary Science Letters* 201, no. 1 (2002): 187–201, https://doi.org/10.1016/S0012-821X(02)00707-0.

[60] C. R. Ytsma and M. D. Dyar, "Accuracies of Lithium, Boron, Carbon, and Sulfur Quantification in Geological Samples With Laser-Induced Breakdown Spectroscopy in Mars, Earth, and Vacuum Conditions," *Spectrochimica Acta B* 162 (2019): 105715, https://doi.org/10.1016/j.sab.2019.105715.

[61] A. M. Ollila, H. E. Newsom, B. Clark III, et al., "Trace Element Geochemistry (Li, Ba, Sr, and Rb) Using Curiosity's ChemCam: Early Results for Gale Crater From Bradbury Landing Site to Rocknest," *Journal of Geophysical Research: Planets* 119, no. 1 (2014): 255–285, https://doi.org/10.1002/2013JE004517.

[62] M. M. Ashry, "Geochemical Behavior of Lithium in Clay Minerals," *Geochimica et Cosmochimica Acta* 37, no. 10 (1973): 2258–2449, https://doi.org/10.1016/0016-7037(73)90120-1.

[63] U. E. Horstmann, "Lithium in Clay Minerals," *Geochimica et Cosmochimica Acta* 11, no. 4 (1957): 215–219, https://doi.org/10.1016/0016-7037(57)90025-8.

[64] H. C. Starkey, "The Role of Clays in Fixing Lithium," *U.S. Geological Survey Bulletin* (p. 1278-F, https://doi.org/10.3133/b1278F.

[65] M. Zawidzki, "The Role of Lithium in Clay Minerals," *Geochimica et Cosmochimica Acta* 40, no. 4 (1976): 587–594, https://doi.org/10.1016/0016-7037(76)90035-7.

[66] O. Ajouyed, C. Hurel, M. Ammari, and N. Marmier, "Removal of Ag+ From Water Environment Using a Novel Magnetic Thiourea-Chitosan Imprinted Ag+," *Journal of Hazardous Materials* 194 (2011): 193–201, https://doi.org/10.1016/j.jhazmat.2011.07.080.

[67] A. Villumsen and O. B. Nielsen, "The Influence of Palaeosalinity, Grain Size Distribution and Clay Minerals on the Content of B, Li and Rb in Quaternary Sediments From Eastern Jutland, Denmark," *Sedimentology* 23, no. 6 (1976): 845–855, https://doi.org/10.1111/j.1365-3091.1976.tb00112.x.

[68] L. B. Williams and R. L. Hervig, "Lithium and Boron Isotopes in Illite-Smectite: The Importance of Crystal Size," *Geochimica et Cosmochimica Acta* 69, no. 24 (2005): 5705–5716, https://doi.org/10.1016/j.gca.2005.08.005.

[69] J. D. Vine, "Where is the Lithium? U.S," *Geological Survey Bulletin* 1831 (1980): 31–39, https://doi.org/10.3133/b1831.

[70] V. Payre, C. Fabre, A. Cousin, et al., "Alkali Trace Elements in Gale Crater, Mars, with ChemCam: Calibration Update and Geological Implications," *Journal of Geophysical Research: Planets* 122, no. 3 (2017): 650–679, https://doi.org/10.1002/2016JE005201.

[71] R. Y. Sheppard, J. M. Weber, L. E. Rodriguez, C. Trejo, E. M. Hausrath, and L. M. Barge, "The Effect of Clay Minerals on Li in Martian Groundwater Simulant," *Icarus* 443 (2026): 116769.

[72] S. H. Markússon and A. Stefánsson, "Geothermal Surface Alteration of Basalts, Krýsuvík Iceland—Alteration Mineralogy, Water Chemistry and the Effects of Acid Supply on the Alteration Process," *Journal of Volcanology and Geothermal Research* 206, no. 1-2 (2011): 46–59.

[73] L. L. Baker, W. C. Rember, K. F. Sprenke, and D. G. Strawn, "Celadonite in Continental Flood Basalts of the Columbia River Basalt Group," *American Mineralogist* 97, no. 8-9 (2012): 1284–1290.

[74] M. Y. Zolotov and M. V. Mironenko, "Chemical Models for Martian Weathering Profiles: Insights Into Formation of Layered Phyllosilicate and Sulfate Deposits," *Icarus* 275 (2016): 203–220, https://doi.org/10.1016/j.icarus.2016.04.011.

[75] C. D. Richardson, N. W. Hinman, L. J. McHenry, J. M. Kotler, D. L. Knipe, and J. R. Scott, "Secondary Sulfate Mineralization

and Basaltic Chemistry of Craters of the Moon National Monument, Idaho: Potential Martian Analog," *Planetary and Space Science* 65, no. 1 (2012): 93–103, https://doi.org/10.1016/j.pss.2012.02.002.

[76] N. J. Tosca, S. M. McLennan, D. H. Lindsley, and M. A. Schoonen, "Acid-Sulfate Weathering of Synthetic Martian Basalt: The Acid Fog Model Revisited," *Journal of Geophysical Research: Planets* 109, no. E5 (2004): https://doi.org/10.1029/2003JE002218.

[77] M. C. McCanta, M. D. Dyar, and A. H. Treiman, "Alteration of Hawaiian Basalts Under Sulfur-Rich Conditions: Applications to Understanding Surface-Atmosphere Interactions on Mars and Venus," *American Minerologist* 99, no. 2-3 (2014): 291–302.

[78] C. Fabre, A. Cousin, R. C. Wiens, O. Gasnault, and S. Maurice, "In Situ Calibration Using Univariate Analyses Based on the Onboard ChemCam Targets: First Prediction of Martian Rock and Soil Compositions," *Spectrochimica Acta Part B: Atomic Spectroscopy* 99 (2014): 34–51, https://doi.org/10.1016/j.sab.2014.03.014.

[79] L. Xiong, J. Hu, S. Yu, M. Wu, B. Xu, and C. Ouyang, "Density Functional Theory Prediction of $Mg_3N_2$ as a High-Performance Anode Material for Li-Ion Batteries," *Physical Chemistry Chemical Physics* 21, no. 13 (2019): 7053–7060, https://doi.org/10.1039/C8CP07398H.

[80] A. C. Allwood, L. A. Wade, M. C. Foote, et al., "PIXL: Planetary Instrument for X-ray Lithochemistry," *Space Science Reviews* 216, no. 8 (2020): 134, https://doi.org/10.1007/s11214-020-00767-7.

[81] M. Movsisyan, E. I. P. Delbeke, J. K. E. T. Berton, C. Battilocchio, S. V. Ley, and C. V. Stevens, "Taming Hazardous Chemistry by Continuous Flow Technology," *Chemical Society Reviews* 45, no. 18 (2016): 4892–4928, https://doi.org/10.1039/C5CS00902B.

[82] K. Gilmore and P. H. Seeberger, "Continuous Flow Photochemistry," *The Chemical Record* 14, no. 3 (2014): 410–418, https://doi.org/10.1002/tcr.201402035.

[83] T. Noël, "A Personal Perspective on the Future of Flow Photochemistry," *Journal of Flow Chemistry* 7, no. 3-4 (2017): 87–93, https://doi.org/10.1556/1846.2017.00022.

[84] L. Buglioni, F. Raymenants, A. Slattery, S. D. Zondag, and T. Noël, "Technological Innovations in Photochemistry for Organic Synthesis: Flow Chemistry, High-Throughput Experimentation, Scale-Up, and Photoelectrochemistry," *Chemical Reviews* 122, no. 2 (2021): 2752–2906, https://doi.org/10.1021/acs.chemrev.1c00332.

[85] D. Webb and T. F. Jamison, "Continuous Flow Multi-Step Organic Synthesis," *Chemical Science* 1, no. 6 (2010): 675–680, https://doi.org/10.1039/C0SC00381F.

[86] S. V. Golubev, A. Bauer, and O. S. Pokrovsky, "Effect of pH and Organic Ligands on the Kinetics of Smectite Dissolution at 25 C," *Geochimica et Cosmochimica Acta* 70, no. 17 (2006): 4436–4451, https://doi.org/10.1016/j.gca.2006.06.1557.

[87] S. D. Domagal-Goldman, et al., "The Astrobiology Primer v2.0," *Astrobiology* 16, no. 8 (2016): 561–653, https://doi.org/10.1089/ast.2015.1460.

[88] I. S. Foster, P. L. King, B. C. Hyde, and G. Southam, "Characterization of Halophiles in Natural MgSO4 Salts and Laboratory Enrichment Samples: Astrobiological Implications for Mars," *Planetary and Space Science* 58, no. 4 (2010): 599–615, https://doi.org/10.1016/j.pss.2009.08.009.

[89] A. Pontefract, T. F. Zhu, V. K. Walker, et al., "Microbial Diversity in a Hypersaline Sulfate Lake: A Terrestrial Analog of Ancient Mars," *Frontiers in Microbiology* 8 (2017): 1819, https://doi.org/10.3389/fmicb.2017.01819.

[90] A. Szynkiewicz, A. P. Johnson, and L. M. Pratt, "Sulfur Species and Biosignatures in Sulphur Springs, Valles Caldera, New Mexico—Implications for Mars Astrobiology," *Earth and Planetary Science Letters* 321 (2012): 1–13, https://doi.org/10.1016/j.epsl.2011.12.015.

[91] S. Góbi and Á. Kereszturi, "Analyzing the Role of Interfacial Water on Sulfate Formation on Present Mars," *Icarus* 322 (2019): 135–143, https://doi.org/10.1016/j.icarus.2019.01.005.

[92] H. G. Changela, E. Chatzitheodoridis, A. Antunes, et al., "Mars: New Insights and Unresolved Questions," *International Journal of Astrobiology*. 20, no. 6 (2021): 394–426, https://doi.org/10.1017/S1473550421000276.